MSc Chemistry

Science for Energy and Sustainability

Master Thesis

Quantification of Ion migration in Perovskite solar cells with varying grain size

---

by

Isabel

Koschany

Stud. nr.: 2656429

June 2020
48ECTS
November20
19 -June2020

Supervisor/Examiner:

Dr. Bruno Ehrler

Examiner:

Asst. Prof. Dr. Rene M. Williams

AMOLF physics of functional complex matter

Hybrid
solar
cells

Abstract:

Metal halide perovskites as an active layer for solar cells gained enourmes attention in the last decade. This is mostly due to their steep increase in efficiency over a short period of time.[1] The interest and research is triggered due to their potential for low cost, large area and flexible solar cell application possibilities. One of the main hurdles preventing perovskite solar cells to be implemented commercially is their instability, which is attributed to ion migration. The fundamental mechanism of ion migration in perovskites is not yet fully understood. For instance, the pathway where ions migrate, inside the grain or at the grain boundaries is still debated. A detailed understanding is crucial for the device fabrication of stable solar cells. Various ways of measuring ion migration are described in the literature. Both theoretical and experimental attempts show a large variety of results. In this work we synthesise $MAPbBr_3$ solar cells with varying grain size and measure the ion migration. Like this we can investigate the influence of the grain size on to ion migration. With the transient ion drift (TID) technique we can determine the sign of charge of the moving ion, the activation energy, the diffusion coefficient, and the ion concentration. Our results show that only Br^- ions are migrating in $MAPbBr_3$ solar cells. We find that ion migration is enhanced at the grain boundaries because we measure a decrease in activation energy with decreasing grain size. For large grains we find an additional pathway for ions to migrate, which we suggest is within the grain. This pathway exhibits a higher activation energy. For more stable perovskite solar cells (PSC) we suggest to direct research towards grain boundary passivation.

2

Contents

1. Introduction

Since the outbreak of SARS-CoV-2 in the beginning of the year 2020 and the following lockdown of several countries, multiple natural healing phenomena have occurred. The sudden decrease in emissions due to the shutdown of large parts of industry worldwide resulted in cleaner air and water in cities. For instance, the Himalaya mountain range was visible again from the northern Indian state of Punjab for the first time within decades, while in Venice, fish were visible again in the canals. This gave us an impression of how our daily lives could be improved, when reducing our emissions in the future.

To achieve a drastic decrease in emissions the origin of energy production must be shifted towards renewables. The sun's irradiance reaching the earth's surface is about 1000 W/m^2 but varies heavily with the location, time of the day and year. To be able to harness this energy in a clean way, solar cell technologies are required. The solar photovoltaic is the fastest growing energy technology in the world.[2] In the last 40 years several solar cell technologies were implemented into the continuously growing market. But in the year 2018 only 3.9% of the European gross electricity output is supplied by photovoltaics.[3] To increase this value, we need to implement solar cell technologies more quickly into more sections of our daily lives. Therefore, we need to enhance the efficiency to increase the value of solar cells. Hence perovskites are very promising because of their potential for low cost, large area, and flexible application possibilities. Until now though commercialization of perovskite solar cells was not reached. One of the main reasons for that is their instability. Perovskites are both ion and electron conductive, which enables ions to migrate and leads to degradation of the devices. Unlike extrinsic degradation factors, like humidity or oxygen, ion migration as intrinsic property cannot be resolved through encapsulation. The fundamental mechanism of ion migration in perovskites is not yet fully understood, for instance the question whether the ions migrate at the grain boundaries or inside the grain has not been fully answered so far.

It has been shown that samples with bigger grains exhibit a lower degradation rate[4] and a higher efficiency[4,5] compared to samples with smaller grains, which suggests that ion migration might occur at the grain boundaries. To get a better insight into ion migration and therefore the instability of perovskite solar cells the migration must be quantified depending on its pathway. In this work we measure the ion migration with Transient Ion Drift (TID)[6] of samples with varying grains size. The varying grain size is a tool to vary the ratio between the area of the bulk and the boundary, which enables us to determine the influence of the grains and grain boundaries on migrating ions. With TID we can determine the activation energy, the diffusion coefficient as well as the sign of charge and concentration of the migrating species. This gives

us insight whether the ion migration is suppressed or promoted inside the grain or at the grain boundaries.

2. Background

2.1. Solar cells

The photovoltaic effect is the theoretical foundation to transform sunlight into electrical current. It describes a phenomenon in which voltage and current is generated due to the absorption of electromagnetic radiation by a semiconductor. A solar cell is a device which is making use of this effect to power an external circuit.

The process in a solar cell can be described by three steps: 1. Creation of charge carriers due to absorption of photons, 2. Separation of charge carriers and 3. Extraction of charge carriers. We descrive these three processes below:

1. Creation of charge carriers due to absorption of photons:

The p-n junction in a solar cell has a band structure as depicted in Figure 1. The p-n-junction is created by doping the semiconductor, the p (positive) side contains an excess of holes while the n (negative) side contains an excess of electrons. It allows current to pass through into only one direction and blocks it in the other. When a photon hits the solar cell, it can either be reflected, pass right through the cell or it can be absorbed. A photon gets absorbed if the energy is higher than the band gap value, which is the energy difference between the valence and conduction bands. The electron gets excited into the conduction band which creates a hole in the valence band. The electron in the conduction band is now free to move and can be extracted.
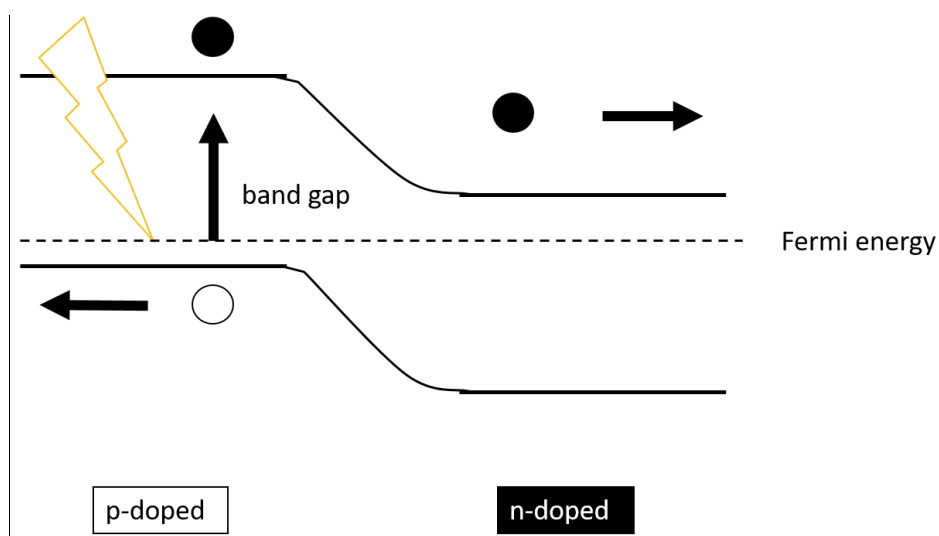

Figure 1: Description of the photovoltaic effect in the band structure of a solar cell

The sun's solar spectrum reaching the earth's surface is approximately a black-body spectrum at 5800K. It is composed of blue photons with an energy greater than the bandgap and red photons with an energy below the bandgap. The red photons cannot be absorbed due to their below-bandgap energy level, while the blue photons do get absorbed in a solar cell, but their excess energy is lost to heat. These issues are major losses to the solar cell efficiency.

2. Separation of charge carriers

Usually the electron hole-pair would recombine shortly after its creation, while releasing the energy in form of another photon or in form of lattice vibrations or it transfers the energy to another electron or hole. But due to the p-n junction the electron in the conduction-band is drawn to move to the n-doped side of the semiconductor due to the lower energy level there. Thus, the energy stored in an electron-hole-pair does not get transformed into heat or radiation but can be used to power an external circuit.

3.Collection of the photo-generated charge carriers

In a last step the charge carriers are extracted from the solar cell by electrical contacts on both sides of the cell. Now, the electrical power generated from sun light can be used in an electricity grid to power our daily lives.

The technology is dominated by silicon (Si) solar cells, with a history of 4 decades in research it presents 90% of the current solar cell market. Even though, Si solar cells are already employed, there is an urgent need for new technologies to be able to supply a larger percentage of the net electricity from solar power. The efficiency and implementation possibilities must be enhanced. For example, Si- solar cell panels are mainly employed at roof tops or fields. Because of the required minimum thickness of silicon solar cells, they are not suited to be implemented on curved surfaces. Perovskite solar cells on the other hand have to potential for highly efficient, thin, and flexible panels, which enables a large variety of implementation locations. This could be key to increase the percentage of electricity supplied by solar cell technologies.

2.2. Perovskites as material for optoelectronic devices

Next to silicon, a variety of other materials like GaAs, CIGS and perovskites have been extensively researched as active layers for solar cells. There has been a lot of excitement about perovskite solar cells in the last 10 years, because of its rapid increase in efficiency, which is depicted in Figure 2.[7] The efficiency of Perovskite Solar Cells (PSC's) reached a record high of 25.2 % within one decade, which is the steepest increase in efficiency of any kind of solar cell so far. Perovskites show a range of positive characteristics like very cost-efficient synthesis methods, long diffusion lengths, long carrier lifetimes and bandgap tunability, all of which gives this material its multiple application possibilities as solar cells, light emitting diodes (LED's) or scintillators.[8] [9,10]
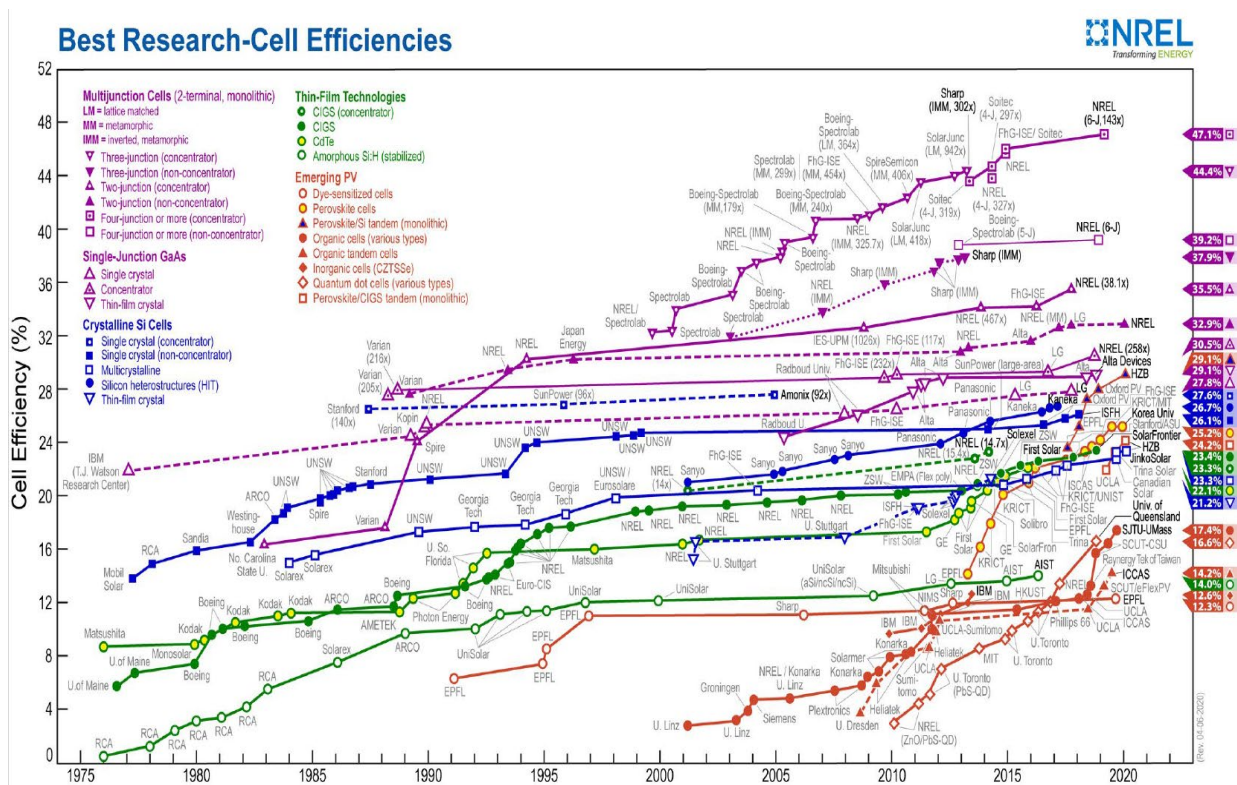

Figure 2: NREL efficiency chart, list of solar cells technologies and their efficiencies. Figure from ref. 1

Perovskite is a class of crystal structures with the formula ABX_3. The A-cation is occupied in a cubo-octahedral site, and the B-cation is occupied in an octahedral site. In many naturally occurring minerals the X-anion is a divalent O^{2-} -ion and the A-and B site are di- and tetravalent, respectively (see Figure 3). The type of perovskite used for solar cell applications has a monovalent halogen ion at the X-site, therefore the A-and B-sites are mono- and divalent like.[11] For solar cell application mostly lead halide perovskites are employed, though there

9

have been attempts to explore lead-free perovskites for solar cell applications such as chalcogenide perovskites.[12] In general, the perovskite structure can be realised by numerous combinations of different ions as far as the charge neutrality condition is satisfied.[13] This wide variation in composition is a key element to understand why perovskites are extensively explored as optoelectronic materials. The most researched perovskite material for solar cell applications is methylammonium lead triiodide ($MAPbI_3$, often abbreviated as MAPI), where the A-site consist of an organic material.[11] This is one interesting property of lead halide perovskites: inorganic materials can be combined with organic materials. Therefore, the organic properties like solubility and cheap synthesis is being combined with the characteristic ionic bonding of inorganic materials.
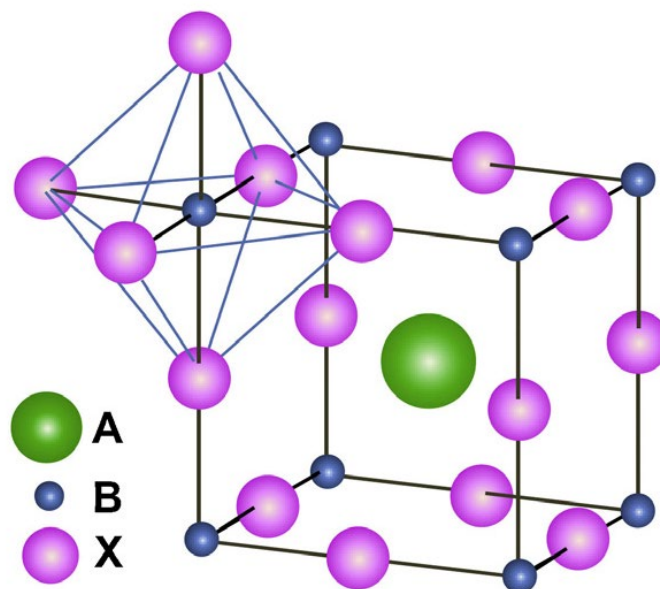

Figure 3: crystal structure of Perovskites ABX_3 [11]

The typical device architecture differs from the traditional Si-solar cell. In perovskite solar cells (PSC's) there are two types of device architectures, the normal n-i-p (n-doped-intrinsic-p-doped) and the inverted p-i-n (p- doped-intrinsic-n-doped) conformation in respect to the order of depositing layers (see Figure 4). The standard depositing layout is glass/TCO/ETL/perovskite/HTL/metal and the inverted layout is glass/TCO/HTL/perovskite/ETL/metal, where ETL refers to the electron transporting layer and HTL the hole transporting layer. The metal contact is commonly made of Au or Ag electrodes and the TCO is a transparent conducting oxide such as indium tin oxide (ITO) or fluorine doped tin oxide (FTO).[8]
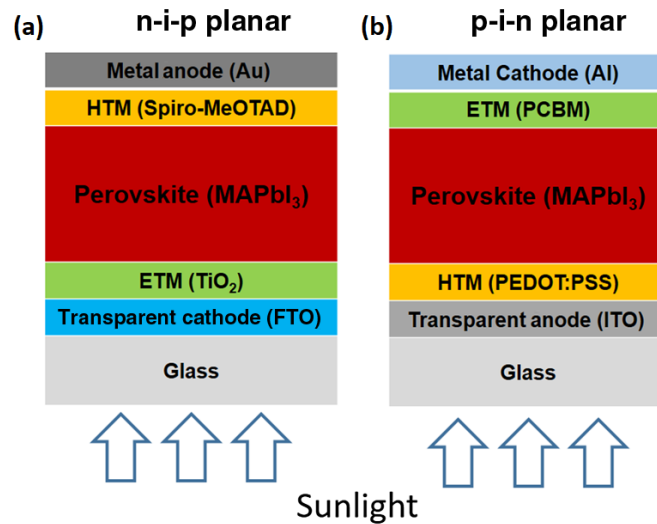
10

Figure 4: device architectures for PSC (a) regular n-i-p and (b) inverted p-i-n orientation. Figure from ref. [14]

To realise these different layers (TCO, HTL, perovskite, ETL, electrode) of the PSC's, either solution processing techniques or vapour deposition techniques are applied. Specifically, the most common way to deposit the perovskite layer is to spin coat, in one or two steps, the precursor(s) directly onto the transporting layer. Another more recently developed technique is the co-evaporation of both precursors onto the substrate.[8]

Primarily PSCs show a high optical absorptivity due to s-p antibonding coupling which results in a high theoretical efficiency threshold. Moreover, lead halide perovskites exhibit a very high absorption coefficient with a sharp offset. In comparison to Si solar cells, PSCs have a direct band gap which leads to the high absorption coefficient and sharp offset, in the range of a photon energy from 1.4 eV to 2.3 eV the absorption coefficient of MAPI is several magnitudes higher than the one for a-Si (see Figure 5).[15]
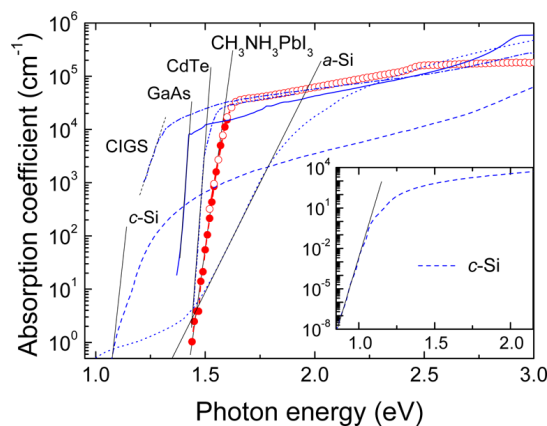

Figure 5: Effective absorption coefficient of a MAPI perovskite thin film compared to other typical photovoltaic materials like amorphous silicon(a-Si),GaAs, CIGS, CdTe, and crystalline silicon (c-Si), all measured at room temperature. Figure form ref. [15]

PSC's show long diffusion lengths of electrons and holes. This gives an advantage when extracting charge carriers. Additionally, PSC's showed a low recombination rate and a high tolerance surpassing structural defects, which decreases the amount of electronic losses.[16,17] Another superior property of PSC's is their bandgap tunability. By replacing the A-site cation completely or partially with other cations, the bond length and angle gets altered which changes the crystal structure and therefore the bandgap slightly. Another way to alternate the bandgap even more is by replacing the halogen atom completely or partially, and by changing the metal.[8,18] This enables a variety of combination possibilities which are depicted in Figure 7. The bandgap can be tuned from 1.15 eV up to 3.06 eV, i.e. from 1050nm to 410nm (see Figure 6).[19]
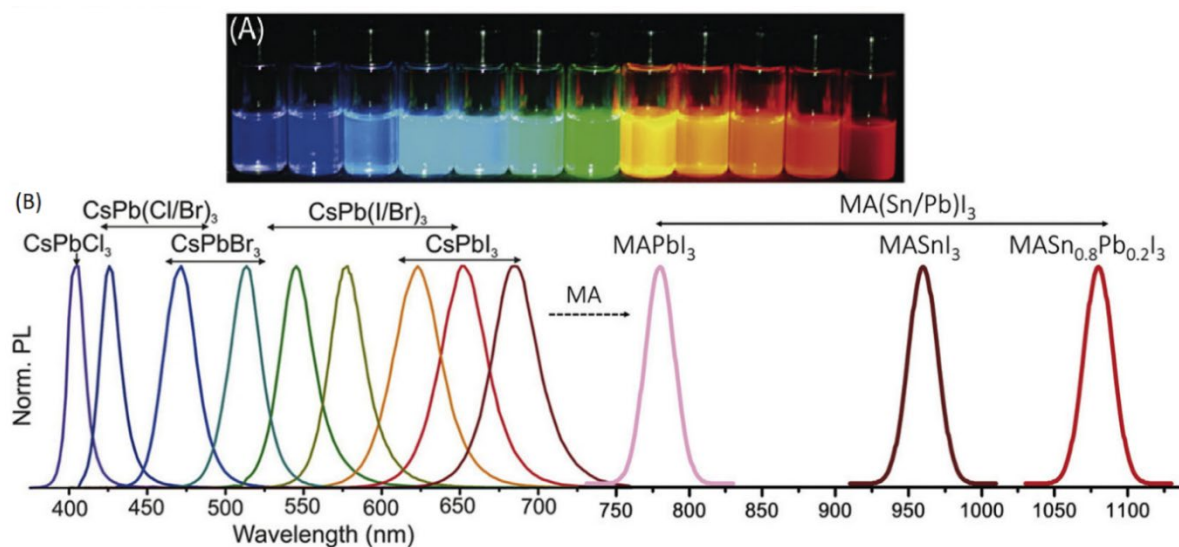

Figure 6: Band gap tunability of perovskites with the structure ABX_3 ranging from 1.15eVto 3.06 eV (a) colloidal library of $CsPbX_3$ (x=cl, Br, I) solutions under UV light (b) representative PL spectra of $CsPbX_3$ extended to $MA(Sn/Pc)I_3$ perovskites. Figure from ref.[19]

Even though PSCs show a range of positive properties, large scale market implementation has not been reached yet. Full understanding of PSCs is indeed necessary for their commercialisation, which is not the case as many areas of limited understanding remain in the field of perovskites. An example of this is the still debated J-V hysteresis, and the lack of long-term stability. The stability of PSCs cannot yet compete with the long lifetime of silicon solar cells. The lifetime of PSC gets substantially reduced by moisture, heat, and UV irradiation.[20] Figure 7 shows the power conversion efficiency (PCE) of PSC against their stability for cells stored under constant illumination of 1 sun.[21] Cells with a high efficiency show only moderate stabilities. The highest stability reported for a highly efficient PSC, with a PCE of around 20 %, is about 1800 h. To tackle the problem of stability many factors have to be considered, not only in the active material but the device structure, design, interlayers and contact materials.[20] Several degradation mechanisms have been elucidated, which gave insight into solution strategies like encapsulation or interfacial engineering.[20,22] One of the main

reasons for the internal degradation of the perovskite layer is ion migration, which is in comparison to degradation due to humidity and oxygen, not resolvable by encapsulation.
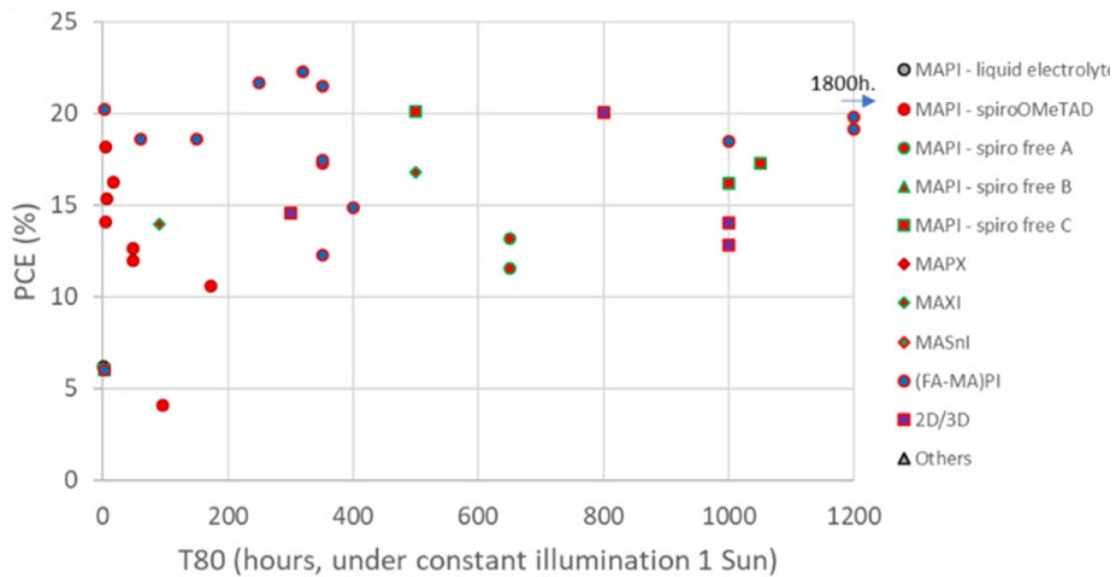
Figure 7: Relationship between PCE and stability for different kinds of perovskite solar cells under constant illumination of 1 sun. Figure from ref. [21]

Furthermore, ion migration leads to another effect called J-V hysteresis, which occurs in the measurement of the photocurrent to voltage curve (J-V-curve). It was found that the PCE depends drastically on the scanning speed and direction, as is depicted in Figure 8.[23] Several explanations were proposed to understand the cause of the hysteretic behaviour in PSCs, such as ion migration[24] , ferroelectricity [25] or an unbalanced charge collection rate[26]. Multiple studies suggested that ion migration is one of the main reasons for hysteresis, this was confirmed by theoretical calculations and microscopic modeling.[24,27]

Figure 8: J-V curves for a MAPbI₃ device for different sweet rates from 0.9 V to -0.3 V and back. Figure from ref.28

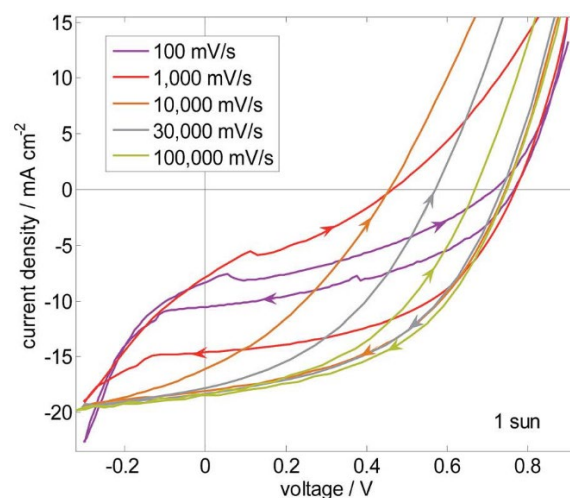## 2.3. Ion migration in perovskite solar cells

A unique aspect of PSC compared to other solar cell technologies lies in the nature of the chemical bonding. Whereas silicon, GaAs or CIGS technologies rely on covalent bonds, perovskites are formed through ionic bonding. In ionic materials some ions are mobile and contribute or even dominate charge transport. One example of such an ionic conductor is AgI, in which positively charged silver ions redistribute in the material according to an external field.[29] In solid materials ionic conductivity is generally described with the Einstein relation.

$$D_{ion} = \frac{k_B T}{q} \mu_{ion}(T)$$

Where D_{ion} is the diffusion coefficient, μ_{ion} is the ionic mobility, k_B is the Boltzmann constant, T is the Temperature, and q is the elementary charge. The nature of the ionic bonding between atoms in a perovskite lattice facilitates defect formation. Due to the implementation of defects, the energetic landscape in the crystal lattice changes, which results in mobile ion species. Mobile ions can then hop from one crystal lattice site to another. This hopping process requires a specific activation energy depending on the route and kind of mobile ion. In the case of materials relevant for PSCs like MAPI and its related halogen variations, multiple examples of halide mobility have been shown.[30] The temperature-dependent diffusion coefficient of the hopping process from site to site of mobile ion species in PSC can be described as the following:

$$D_{ion} = D_0 \exp\left(\frac{-E_a}{k_B T}\right)$$

Where D_0 is a temperature independent pre factor and E_a the activation energy the ion must overcome to hop from on site to another. Ion migration results in several disadvantages for PSCs, on top of hysteresis it has been shown to be a possible cause for degradation.[31,32] Ion migration as an intrinsic effect cannot be resolved by encapsulation, thus it is important to understand its mechanism and pathways to be able to direct the research towards more stable PSCs. On the other hand, ion migration can also be an opportunity for further applications like memory resistors or switchable diodes.[28] In the following section, the concept of ion migration in PSCs will be explained on an example perovskite ABX_3, where A is a monovalent cation such as MA$^+$ or FA$^+$, B is a divalent cation like Pb^{2+} and X is a monovalent halide anion such as I$^-$ or Br$^-$. There are three main kinds of intrinsic point defects which can occur in the crystal lattice of perovskite solar cells (see Figure 9): vacancies where one place in the lattice stays empty, interstitials when an ion is placed between the crystal lattice sites, and antisites when two ions are interchanged. Depending on the way they are formed, these defects can be divided into two subcategories, Schottky and Frenkel defects. The most common neutral ones

are Frenkel defects, which are defects that occur paired e.g. when an interstitial defect leaves a vacancy behind. Schottky defects are unpaired, for example charged defects like an X⁻ vacancy. Defects as well as ions can migrate within the crystal lattice.[28]
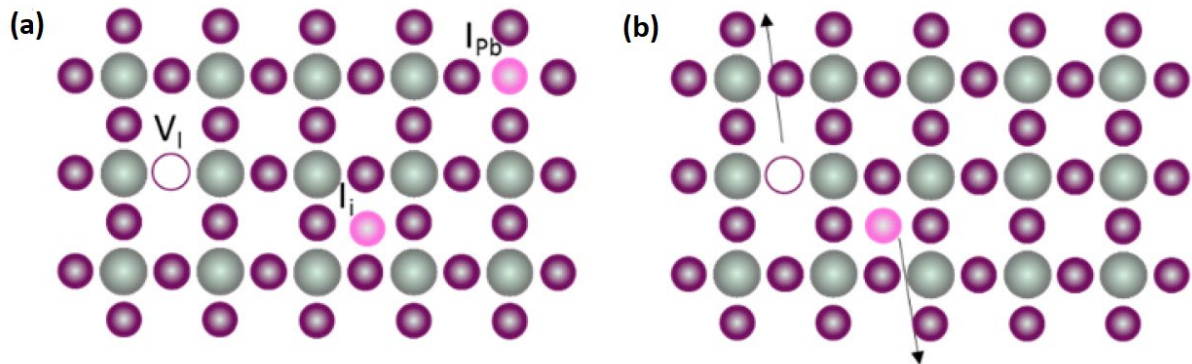
The relevance of a defect is dependent on its mobility and concentration. The formation process of the perovskite film can influence the defect concentration. The activation energy for the migration of defects can be calculated through first principle computational modelling, which has been done extensively for MAPI, as shown in Table 1.[33] The reported values are widely spread which makes a comparison of theoretical calculated activation energies difficult. Furthermore, the results from an experimental point of view are also widely spread to differences in the fabrication methods of the samples as well as the experimental conditions.[33] Many experimental methods also fail to distinguish the sign of charge of the migrating ion which leads to misassignment of the ions.[30]

Table 1: Activation energy for ion migration in eV for MAPI[33];

	experimental	theoretical
V_i^+	0.2[34], 0.6[24], 0.3[35]	0.1[27], 0.3[36], 0.6[18], 0.2[30]
I_i^-		0.1[21]
V_{MA}^+	0.4[37]	0.5[21], 0.6[30], 0.8[18], 0.6[30]
V_{Pb}^{2-}		0.8[21], 0.9[30], 2.3[18], 1.4[30]

Some of the measurement techniques used are temperature-dependent transient measurements of an effect which is likely to be caused by ion migration. This is the case for J-V hysteresis[35], chronoamperometry[24], transient photo voltage decay[38], and transient capacitance[30]. Another way to quantify ion migration is spatially resolved probe methods like KPFM[39] or conductivity measurements[40,41]. Several effects other than ion migration, like detrapping of charge carriers, charge accumulation at interfaces,[42] or ferroelectric effects[43,44], can influence these measurements and falsify the results.

2.4. Influence of the grain size on ion migration

Perovskite thin films made by spin coating are polycrystalline. Depending on the synthesis method the size of the grains can vary and therefore the grain to boundary ratio. In films with large grain size, the effects inside the bulk will be more pronounced and in films with small grain size, effects at the boundaries will be more pronounced.[45] The crystal structure close to grain boundaries is different from the structure in the bulk which in turn leads to different energetic landscapes, and therefore different activation energies for ion migration. Theoretically, defects are more likely to be formed at the surface of grains. For example, it is favourable to form an interstitial defect at the grain boundaries, because the steric hindrance is reduced at the surface, and under-coordinated Pb atoms are more likely to bind to the interstitial. This results in lower activation energies for defect formation at the boundary and therefore lower activation energies for the ion migration process at the boundaries rather than within the grain.[46] Defects can also cause an unintentional band bending as shown in Figure 10a. For MAPI, I$^-$ vacancies can create shallow defect levels near the conduction band which can create a local n-type doping, while MA$^+$ or Pb^{2+} vacancies can create shallow defect levels next to the valence band which can create a local p-type doping. This band alignment is more pronounced at the grain boundaries than inside the bulk. Therefore ion migration could be enhanced at the grain boundaries due to a possibly higher diffusivity at the grain surface creating so-called ion migration channels (see Figure 10b).[47,48]
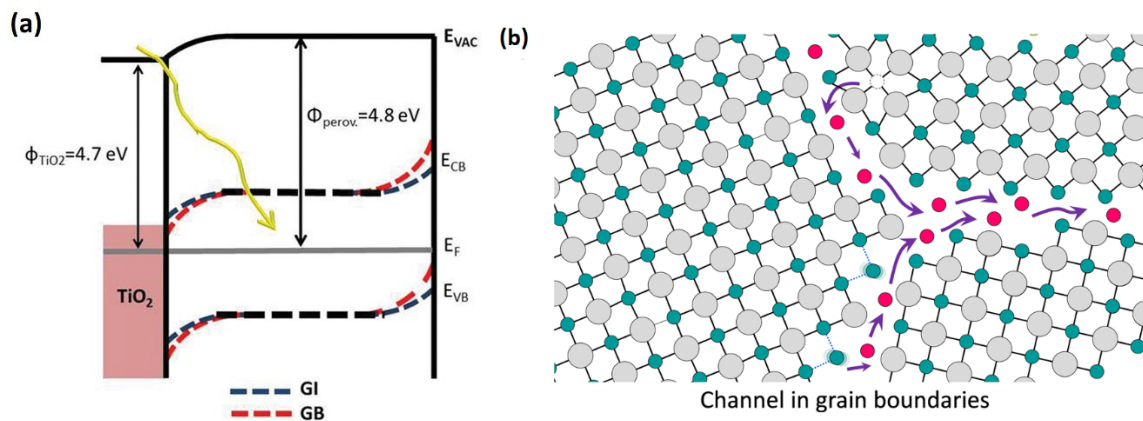
Figure 10: (a) Energy diagram of the perovskite layer under the influence of built-in potential (V_b) , E_{CB} is the conduction band energy, E_{VB} is the valence band energy and E_F is the Fermi level [47] (b) ion migration channel at grain boundaries. Figure from ref. 48

Nie et al. synthesized a PSC with millimetre scale grains which exhibit a high PCE and reduced hysteresis, which strengthens the hypothesis that ion migration occurs mainly at grain boundaries and causes hysteresis.[5] Furthermore Shao et al. reported that ion migration is dominating at the grain boundaries, based on the enhanced hysteresis measured locally on the grain boundary with AFM.[49] Even though a lot of studies[5,49,47] suggest that ion migration

happens mainly at grain boundaries, there is still a lack of research towards quantification of the ion migration process, within grains and at grain boundaries. So far there is no uniform system to measure ion migration without a change in key parameters of the recipe (through the additive, solvent, or antisolvent) that most probably also influence the ion migration, and therefore a lot of varying results were collected. It is essential to quantify ion migration with respect to their pathways in the grain or at the grain boundaries. In this work, we use a fabrication method which allows us to measure ion migration of several films with different grain sizes made from the same batch without changing the solvent, and without any additives but simply changing the spin-coating time. Therefore, we can determine the effect arising specifically from the grain size from any other effects influencing ion migration. The technique we use to quantify ion migration, called transient ion drift, can differentiate between positive and negative ions. This is crucial to avoid mis-assigning the ions. Thus, we can distinguish the influence of the pathway of ion migration, weather inside the grain or at the grain boundary.

3. Methods

In this chapter the methods are described which have been used to synthesise the PSC with varying grain size, to characterize the samples and to measure the ion migration with respect to the grain size.

The table below lists all chemicals which have been used with their origin and purity (see Table 2).

Table 2: List of chemicals used in the synthesis

Material/ Chemical	Molecular Formula	Company of origin	Details
Nickel(II) nitrate hexahydrate	$Ni(NO_3)_2 \cdot 6(H_2O)$	Sigma-Aldrich	99.999% purity
Methyl ammonium hydro bromide	$CH_3NH_2 \cdot HBr$	Sigma-Aldrich	98% purity, low water content
Lead(II) acetate trihydrate	$Pb(CH_3CO_2)_2 \cdot 3H_2O$	Sigma-Aldrich	99.999% purity
Bathocuproine	$C_{26}H_{20}N$	Ossila	99.5% purity
Fullerene	C_{60}	Sigma-Aldrich	99.5% purity
Gold	Au	Kurt J. Lesk	99.99% purity

3.1. Fabrication of the MAPbBr₃ solar cell devices with varying grain size

In this chapter we first describe the device architecture, after that the method to vary the grain size distribution in the perovskite films is described and finally the synthesis is explained in detail.

3.1.1. Device architecture

We chose the device architecture following the approach of Futscher et al.,[30] as it is suitable for ion migration measurements with the TID method. Indeed, to avoid contradicting events in the TID analysis, the p-i-n structure is used because of its reduced charge accumulation and reduced capacitive hysteresis compared to the regular n-i-p structure.[50] The picture below describes the device architecture (see Figure 11). The substrate is a pre synthesised FTO on glass layer. As ETL, we choose nickel(II)-oxide (NiO_x) over the commonly used PEDOT:PSS, because of the latter's tendency to absorb water, which can lead to sample degradation.[51] As absorbing layer we choose MAPbBr₃, because of its ability to easily tune the grain size in the spin coating step, see below. The ETL is the commonly used combination of bathocuproine (BCP)/Fullerene (C_{60}), which are both evaporated on top of the perovskite layer. At final step, the gold (Au) contact is evaporated through an evaporation mask, defining an electrode architecture of 8 pixels per sample.
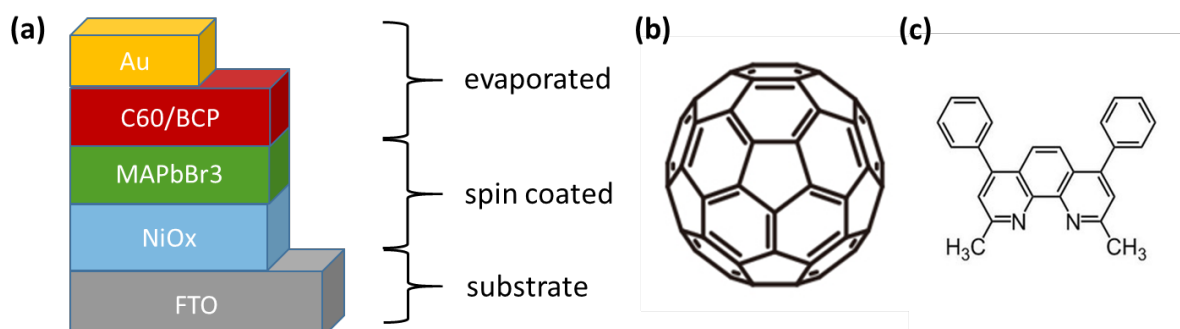
Figure 11: (a) Device architecture of the synthesized PSCs with indication of their synthesis methods (FTO/NiOₓ/MAPbBr₃/C60+BCP/Au),(b) Molecular formula of C60 and (c) BCP

3.1.2. Fabrication

To be able to compare samples with different grain sizes, a method as similar as possible must be used to fabricate the devices. Therefore, we use the method of Adhyaksa et al.[52], a fabrication method for MAPbBr₃ solar cell devices which gives different grain sizes for the perovskite film, when varying only the spin coating parameters. Spin coating is a commonly

known technique for the fabrication of PSC. In this technique, the precursor gets drop casted with a pipet onto the substrate, which is attached to a routable plate. The plate gets spun for a certain time and with a specific speed. During the spinning, part of the precursor solution is removed, and nucleation sites are formed. After the spinning, the samples are heated to a certain temperature. This process is called annealing and it is necessary for the evaporation of the rest of the solvent and for the grain crystallisation and growth (see Figure 12).
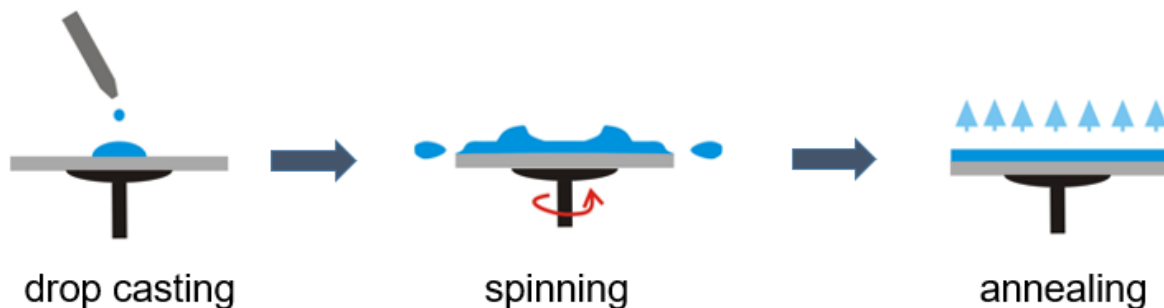
Figure 12: Three steps of spin coating: drop casting, spinning and annealing

In our approach, we keep the spin coating speed and only vary the spin coating time, which allows us to control the nucleation density. Short spin coating times result in a low nucleation density, and therefore large grain sizes, because of the available space for the grains to grow. Long spin coating times result in more nucleation sites, which in turn results in smaller grains, because each grain's growth is rapidly stopped by an adjacent grain (see Figure 13).

Figure 13: Grain size against the spin coating time for different spin coating speeds of 5000 rpm, 7,5000 rpm and 10,000 rpm. Figure from ref. 52

3.1.2.1. Preparation of the samples

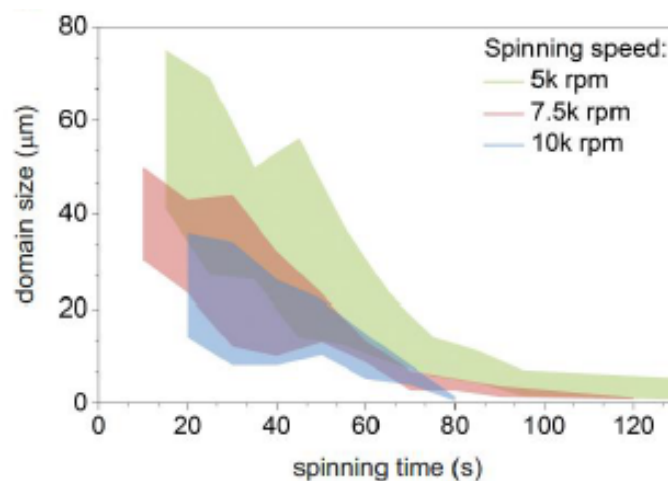As substrate, we use a Glass/FTO plate with an area of 1.5x1.5 cm. To ensure a uniform film formation, the substrate must be cleaned properly in several steps. First, the substrate is brushed with water and soap. After that, the substrate is cleaned three times in the ultrasonicator, with water, acetone, and isopropanol for a duration of 15 minutes. To ensure that every organic material is removed from the surface, the samples are dried with the nitrogen (N_2) gun and placed, the FTO side facing up, into the plasma cleaner for 20 to 25 minutes. After cleaning the substrate, the ETL and perovskite film can be spin coated on top of the conducting FTO side.

3.1.2.2. Spin coating

Spin coating NiO_x:

The precursor for the NiO_x is a 0.3M solution of nickel(II) nitrate hexahydrate dissolved in ethanol. After the powder is dissolved, the solution gets filtered with a 0.45 μm PVDF filter, to prevent nanoparticle formation. The precursor is spin coated and annealed in the fume hood to avoid contamination of the sample. We drop cast 100 μL of solution onto the sample and apply a spin coating speed of 4000 rpm for 15s. Afterwards, the samples are annealed on the hot plate, following a specific temperature treatment. First, the samples are left at 150°C for about 10 to 15 min, before a heat ramp starts, with 3°C/min, until the set value of 350°C is reached and kept for 1h. After this annealing step, the samples are cooled down and put one more time into the plasma cleaner to remove any potential organic contamination on the surface. We then move to the perovskite layer synthesis step.

Spin coating perovskite:

Perovskites are instable in ambient condition, therefore the fabrication of the precursor and the spin coating of the $MAPbBr_3$ precursor is made exclusively in the glove box in nitrogen atmosphere with an oxygen level of less than 1 ppm. The precursor for the $MAPbBr_3$ layer is fabricated from two solutions dissolved together in dimethyl sulfoxide (DMSO). First, a solution of 5.5 M methylamine hydro bromide (MABr) is made by dissolving the powder in DMSO. To ensure a complete dissolution, the precursor is stirred and heated on a hot plate to 50-60°C. The second precursor is a 1.8 M lead(II) acetate trihydrate (PbOAc) solution. To prepare this solution, the PbOAc powder is dissolved in DMSO and stirred and heated to 50-60°C overnight. Both precursor solutions are stirred and heated up to 65°C until a clear dense solution is formed. This final $MAPbBr_3$ precursor solution has a molarity of 3.05M. For the spin coating step, 200 μL are used per sample, with a spin coating speed of 7500 rpm. To vary the grain size in the perovskite film we vary the spin coating times between 5 s, 10 s, 20 s, and

60 s. The samples are annealed for 1 h on the hot plate in the glove box at 70°C. During this annealing step, the samples quickly show a yellow-orange colour, characteristic for MAPbBr$_3$ (see Figure 14).
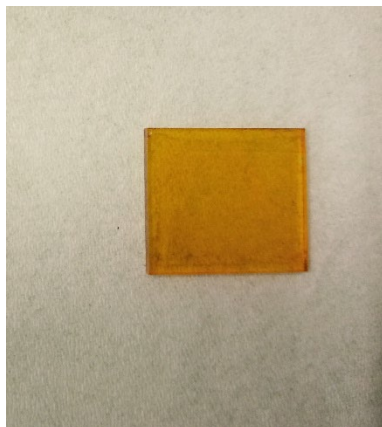

Figure 14: MAPbBr$_3$ thin film on top of a glass substrate with a FTO and NiO$_x$ layer.

3.1.2.3. Evaporating

Once the hole-transporting layer and perovskite layer are prepared, we continue our device fabrication by evaporating the HTL and metal contact on top. Thermal evaporation works in the following way: a material is placed in a source, where it is heated up until it starts evaporating and is deposited with a controlled speed onto the substrate. We use an Angstrom depositing system. The sample holder in the evaporator allows for 16 samples to be evaporated at the same time.

Evaporating C$_{60}$: a 30nm thick C$_{60}$ layer is evaporated on top of the perovskite layer. It is deposited with 0.2 Å/s.

Evaporating BCP: The BCP layer is deposited on top of the C$_{60}$ layer, up to a thickness of 8 nm, with a depositing speed of 0.2 Å/s.

Evaporating Au: Before the Au contact layer is deposited an evaporating mask is put on the samples to define 8 contact pads onto each sample (see Figure 15). The thickness of the metal contact is 120 nm, where the first 10 nm are deposited with a speed of 0.1 Å/s and the rest of the layer with a speed of 1 Å/s. The reduced speed at the beginning of the deposition is necessary to ensure that the temperature remains low enough to avoid ample damage.
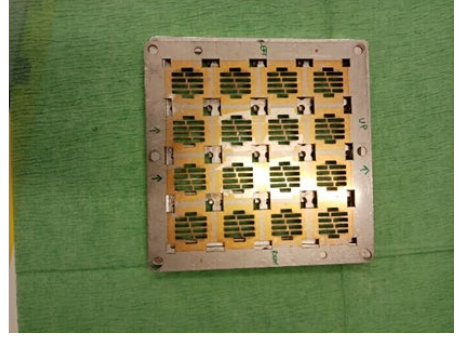
(a)
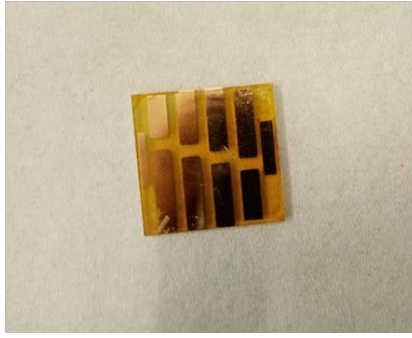
(b)

Figure 15: (a) fully stacked MAPbBr$_3$ solar cell with 8 different pixels and (b) evaporation mask to realize 8 pixel per sample.

24

3.2. Characterisation

This chapter describes the different characterisation methods we used to measure the optoelectronic and structural properties of our PSC. First, we analyse the perovskite layer on its own with XRD and UV-Vis. We analyse then the average grain size of each perovskite layer by using a software tool (ImageJ) on optical microscope images. Finally, we analyse the device operation of the complete solar cell with J-V and EQE measurements.

3.2.1. *Optical and crystallographic properties of the MAPbBr$_3$ perovskite layer*

To be able to analyse the MAPbBr$_3$ layer individually, for every spin coating time, we leave one sample without the ETL and gold contacts. Thus, we can analyse the upper perovskite layer from these samples. To evaluate the absorbance of the perovskite layer, we measure the UV-Vis spectrum. Which is also an indicator for parasitic absorption inside the film. We use a lambda 750 UV/Vis/NR spectrometer from Perkin Elmer. To get more specific information about the crystallographic lattice and potential impurities inside the film, we perform XRD measurements. For this, we use the D2 phaser XRD set up from Bruker. In addition to that we take SEM images of the cross section of our samples to analyse the thickness of the perovskite layer with a Verios 460 high resolution SEM from FEI.

3.2.2. *Analysis of the grain size*

To be able to study the grain-size dependent ion migration in perovskites, a detailed grain size distribution per measured sample is necessary. First, we take pictures of the unfinished samples with the perovskite layer as top layer using an optical microscope. For the largest grain sizes with a spin coating time of 5 s and 10 s, we use a magnification of 20x to 50x. For samples with smaller grain sizes, made with spin coating times of 20 s and 60 s, we use the highest magnification of 100x. To quantify the grain size, we use a software tool to evaluate and analyse the distribution of the grain size of the pixels after they have been measured by TID. This is done by evaluating each grain size from the pictures with the program ImageJ.

3.2.3. *Characterisation of the performance of the MAPbBr$_3$ solar cells*

To ensure that we synthesise working solar cells, we characterize the optoelectronic performance of the samples. To do so, we measure the J-V-curve and the external quantum efficiency (EQE) of the MAPbBr$_3$ devices. The EQE is the ratio of the number of charge carriers collected by the solar cell to the number of incident photons. To measure the EQE, the solar cell is exposed to a light source with varying wavelength and calibrated flux. A current is measured, which can be translated to a number of charges to obtain the EQE value. We analyse the EQE with a Quant X 300 set up from Oriel instruments previously calibrated with

a Si solar cell. Furthermore, the J-V-curve is measured by sweeping the voltage and measuring the resulting current density. This is done, both under dark and illumination conditions. For the illumination we use a solar simulator with an Oriel Sol 2A Newport lamp, with controlled irradiance of 1 sun. The samples were encapsulated while being measured, to prevent degradation from oxygen exposure.

3.3. Transient Ion Drift

In this chapter we describe the transient ion drift technique, explain its theoretical background, and develop the analysis procedure.

3.3.1. Measurement

To measure ion migration a powerful technique, called transient ion drift (TID) was used with which we can identify the charge of mobile ions (anion/cation), their activation energy to migrate, their diffusion coefficient and the charge carrier concentration. The TID technique relies on measuring the capacitance decay for a range of temperatures after applying an external voltage for a specific time.[6] The influence of an external forward bias (V_0) on the band structure is depicted in Figure 16. At short circuit conditions for V=0, the mobile ions accumulate at the interfaces (see Figure 16a). After applying a forward bias which equals the built-in potential, the system is not in equilibrium anymore, thus the ions start migrating through the perovskite layer (see Figure 16b), until they reach equilibrium again (see Figure 16c). After taking away the forward bias, the ions will migrate back to the interfaces, which results in a capacitance decay that can be used to quantify ion migration (see Figure 16d).[30]
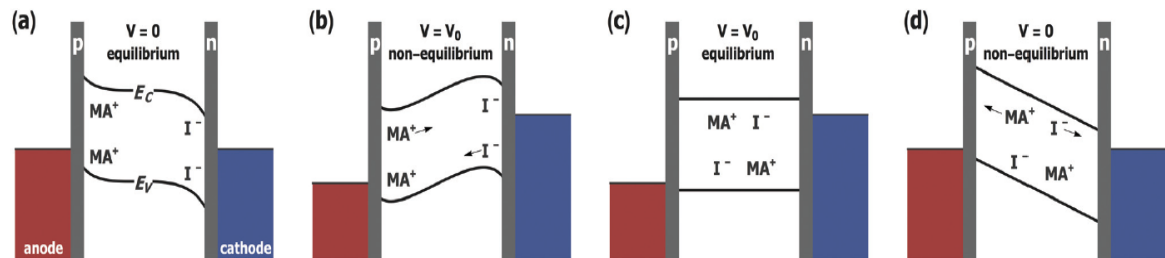

Figure 16: Influence of the voltage pulse on the band energies of MAPbI₃ for (a) in equilibrium at short circuit condition (b) under influence of an applied forward bias V₀, when the ions start to migrate (c) developed equilibrium for an applied voltage bias V₀ and (d) non equilibrium for after removing the voltage bias, when ions migrate back to the interfaces. Figure from ref. 30

Our set-up includes a cryostat (Janis) in which the sample is placed in vacuum and cooled with liquid nitrogen. A Pfeiffer vacuum pump is used to achieve a base pressure of about $2 \cdot 10^{-6}$ mbar. A temperature controller is used to vary the temperature of the sample from 210 K to 340 K, with a resolution of 0.2 K. The set-up includes a pixel switch, which makes it possible to measure multiple pixels without breaking the vacuum. The measurement is controlled by a device from Semetrol, which is able to apply a voltage and measure the capacitance decay for the TID. Furthermore device is able to measure the J/V and C/V-curve, as well as the impedance. The complete set up is depicted in Figure 17.
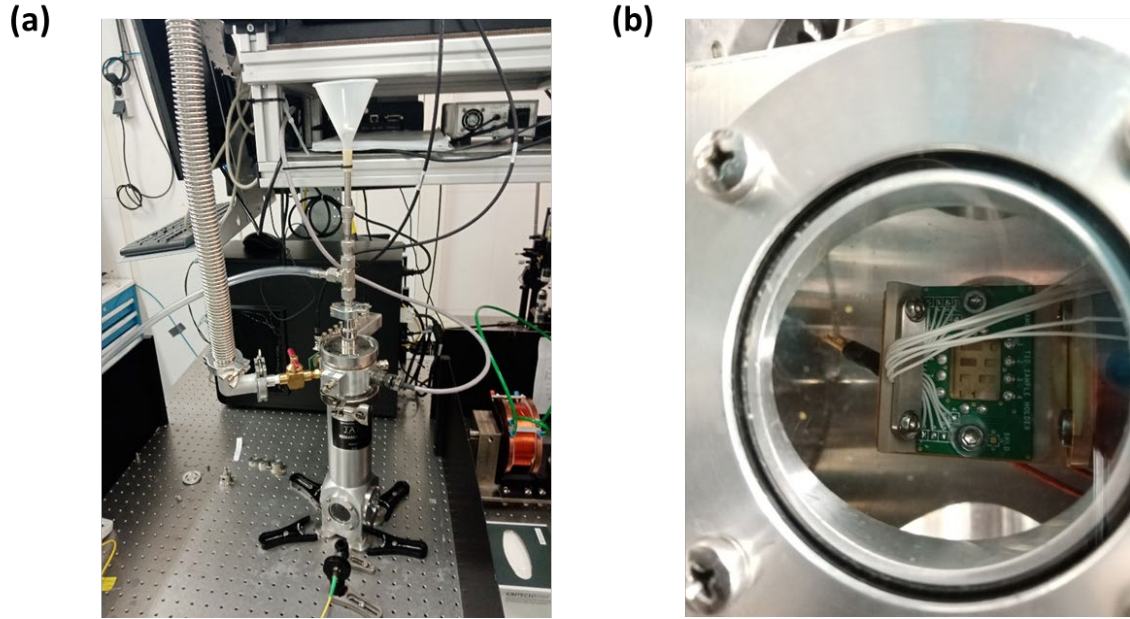
(a)   (b)

Figure 17: Picture of the (a) complete set up of the TID and (b) sample holder inside the cooling cylinder

To obtain important characteristics like the build in voltage V_B, the doping density N_A, and the permittivity of the perovskite film, we performed several test measurements before and after measuring the TID signal. To do this, we determine the impedance, the capacitance to voltage (C-V) curve and the current to voltage curve (I-V). The impedance is measured by applying an AC voltage of 50 mV, varying from 1 Hz to 500 kHz. The C-V curve is measured by applying a voltage varying from -0.2 V to 1.2V (forward and reverse) and an AC voltage of 10mV with a frequency of 10 kHz while measuring the capacitance. With the C-V measurement we can create a Mott-Schottky plot ($1/C^2$ vs. voltage) which provides us information about the built-in voltage V_B and about the charge carrier density N_A, using the following equation:

$$\frac{1}{C^2} = \frac{2}{\varepsilon\varepsilon_0 A^2 q N_A}(V - V_B - \frac{k_B T}{q})$$

Where C is the capacitance, ε is the dielectric constant of the perovskite layer, e_0 is the vacuum permittivity, q is the elementary charge, N_A is the doping density, V is the applied voltage, V_B is the build-in voltage, k_B is the Boltzmann constant and T is the Temperature. The J-V curve is measured by applying voltage in a range from -0.2 V to 1.2 V (forward and reversed) and measuring the resulting current density to check for series, shunt resistances and J-V-hysteresis.

In addition to the TID we measure the transient admittance for each sample. The transient admittance spectroscopy (TAS) can be performed with the same set up as the TID. The TAS is measured by applying an AC voltage of 50mV with a varying frequency from 1 Hz to 500

28

kHz, by varying the temperature from 210 to 350 K, with 10 K steps. The TAS is a second method to calculate the activation energy for ion migration.

Trapping and detrapping of electrons from defect levels also results in a capacitance transient. To measure defect levels a, technique very similar to the TID is used, the deep level transient spectroscopy (DLTS).[53] DLTS measures the capacitance transient on a short time scale of milliseconds, in contrast to ion migration in PSC which happens on a longer time scale of milliseconds to seconds. Measurements with very short filling time (0.2ms) did not result in a capacitance transient, therefore we can assume that the measured capacitance transients in TID results only from ion migration (Figure 18a)

For the TID measurement, the pulse duration necessary to achieve flat bands within the perovskite layer must be determined. To do so, we measure the change in capacitance for different voltage pulse durations. The capacitance difference does not increase substantially for filling pulses longer than 2 s anymore, indicating that a saturation of mobile ion re-distribution is reached. Hence, we choose a pulse duration of 2 s (Figure 18b).

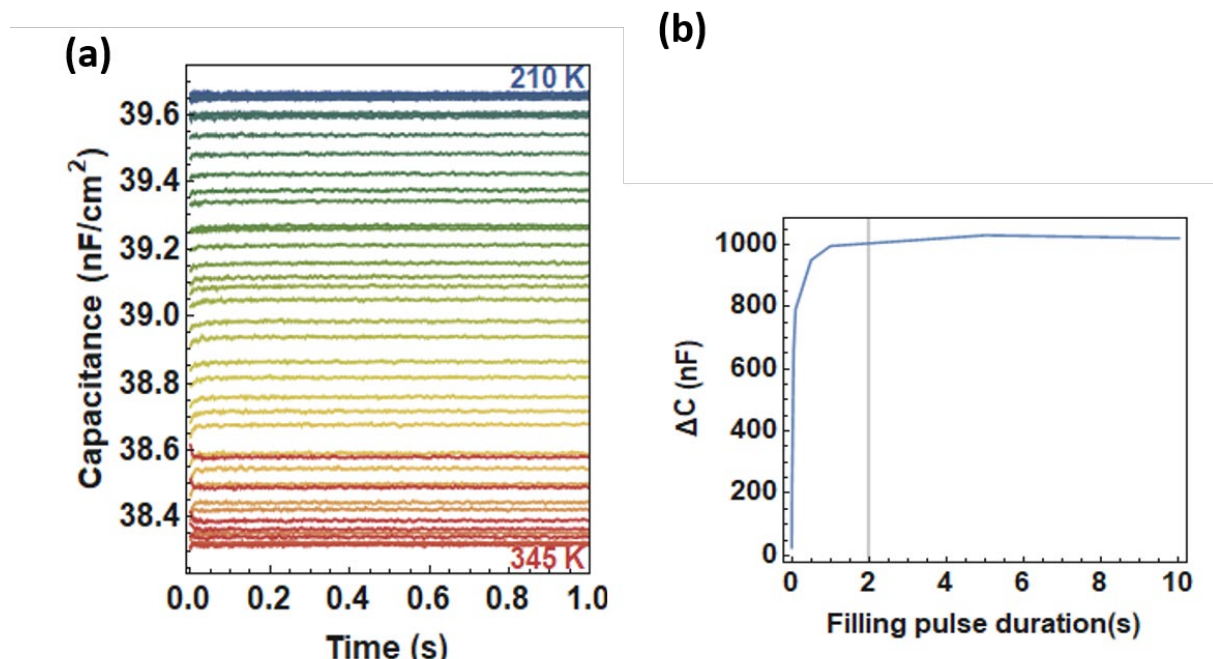*Figure 18: (a) capacitance transients of a sample with a spin coating time of 5s with a filling voltage of 0.2 ms for a temperature range from 210 K to 345K (b) determine the filling pulse duration by measuring the capacitance difference for different filling pulse durations from 1 s to 10 s at room temperature*

3.3.2. Theory

The starting point to understand ion migration is the equation for ion diffusion coefficient:

$$D_{ion} = \frac{v_a d^2}{6} \exp\left(-\frac{\Delta G}{k_B T}\right) = \frac{v_a d^2}{6} \exp\left(-\frac{\Delta S}{k_B}\right) \exp\left(-\frac{\Delta H}{k_B T}\right)$$

Where v_a is the attempt frequency for an ionic jump, d is the jump distance, ΔG the change in Gibbs free energy, ΔS is the change in entropy and ΔH is the change in enthalpy during the jump of the ion. The change in enthalpy can be written as the activation energy for the mobile ion to make a jump. The equation above can be simplified to:

$$D_{ion} = D_0 \exp\left(\frac{-E_a}{k_B T}\right)$$

Where D_0 is a temperature-independent pre-factor. The measured capacitance transients can be described by an exponential equation of the following format:

$$C(t) = C(\infty) \pm \Delta C \exp\left(-\frac{t}{\tau}\right)$$

Where C(∞) is the steady state capacitance which is reached after about 1 s, ΔC is the capacitance difference and τ is the time constant for ion migration given by:

$$\tau = \frac{\omega_D}{\mu E}$$

Where ω_D the depletion layer width, which we assume to be the thickness of the perovskite layer, and μ the mobility of the migrating ions and E the electric field. The electric field can be written as function of the doping density N_A

$$E = \frac{q \omega_D N_A}{\varepsilon_0 \varepsilon},$$

Where q is the elementary charge, ε_0 is the vacuum permittivity and ε is the dielectric constant of the perovskite layer. In combination with the Einstein relation

$$D = \frac{\mu k_B T}{q},$$

the time constant can be written as

$$\tau = \frac{k_B T \varepsilon_0 \varepsilon}{q^2 D N}.$$

The time constant is identified by the fitting procedure for a range of temperatures and is used to calculate to the activation energy and the diffusion coefficient.

3.3.3. Analysis

To identify the migrating species, we fit every temperature decay to an exponential decay, from which we can extract the time constants which we then use to calculate the diffusion coefficient and activation energy. This can be done in two ways, one following the work by Futscher et al[6] fitting each capacitance transient individually and reconstructing the parameters from an Arrhenius plot ("individual fit"), or by a second method which consist in applying a global fit, such that all capacitance transients are fitted with one set of E_a and D.

Individual analysis

In the individual fit, the capacitance transient at every temperature is fitted to an exponential decay using Mathematica. Then, the time constants are implemented in an Arrhenius plot to extract the diffusion coefficient from the y-intersection and the activation energy from the slope of the line. The concentration of the moving ion can be calculated by the fitted value for the capacitance difference ΔC. We fit each temperature transient individually to the exponential function described above. Figure 19 shows an example for the Arrhenius plot and the concentration plot for a typical MAPbBr$_3$ solar cell device, where the upper example (see Figure 19a and 19b) gave reasonable results but the second example shows unphysical results with a negative activation energy (see figure 19c and 19d). The individual analysis of each transient results in different numbers of exponentials per transient which makes the analysis in the Arrhenius plot difficult. We are not able to extract the activation energy for all data sets specifically in cases where the choice between 2 or 3 exponentials is unclear. Therefore, we develop a new method to achieve more conclusive results.
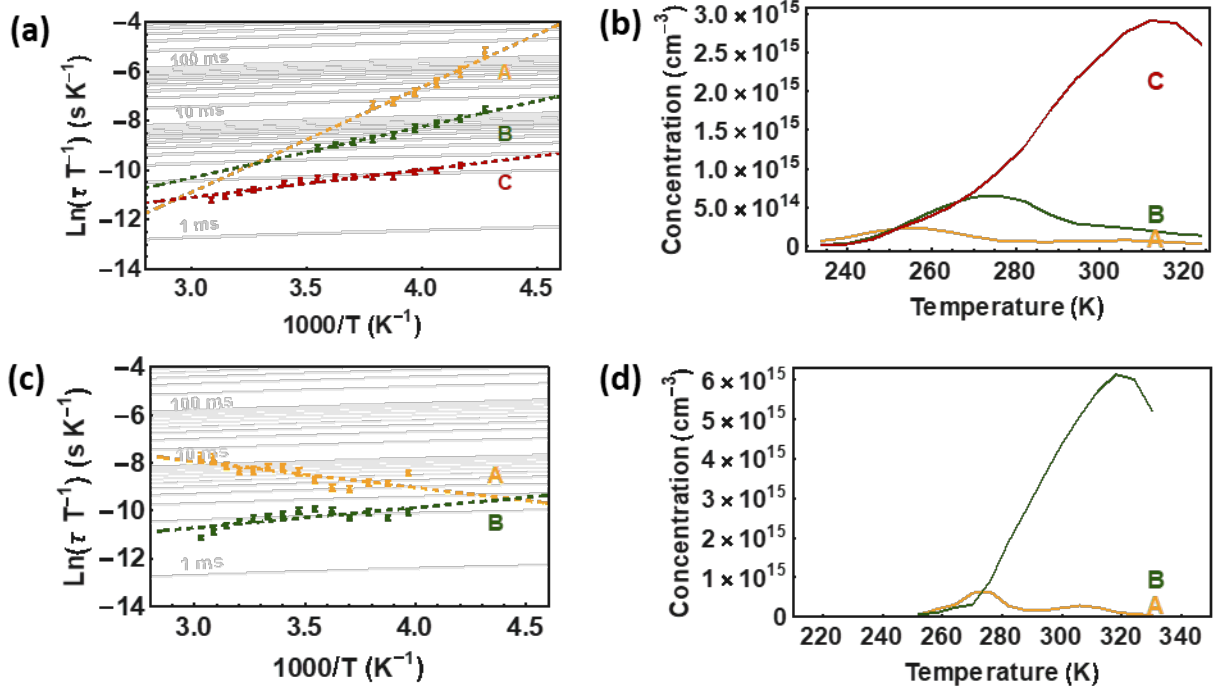
Figure 19: (a) Arrhenius plot and (b) ion concentration for a successful fit for 3 exponentials and (c) a unreasonable Arrhenius plot with (d) the responding ion concentration for a failed fit for 2 exponentials, calculated from the fitted value for the difference in capacitance.

Global analysis:

We develop a new fitting method with the program Igor, which allows us to create a user-friendly interface to globally fit our data. In this process, we fit the complete temperature range to one E_a and one time-constant term from which we can then calculate the diffusion coefficient and ion concentration. We fit the capacitance transients to the following fit function:

$$C(t) = C(\infty)(T) + \Delta C \, exp\left(\frac{-t}{c \, T \, exp\left(\frac{E_a}{k_B \, T}\right)}\right)$$

Where c represents the time constant. The fit function gets extended by an additional term, if a fit with multiple exponentials is necessary. Thus, we add another exponential term with a separate ΔC, E_a and c. The $C(\infty)$ term is extracted from the last points of each capacitance transient, while ΔC/2 is used as a starting value for the fit for ΔC. We link the values for c and E_a to the whole temperature range, while ΔC is fitted individually for each transient. The fit function represents the whole temperature range very accurately for one or two exponentials (see Figure 20a for a fit with 2 exponentials and Figure 20b for 1 exponential).
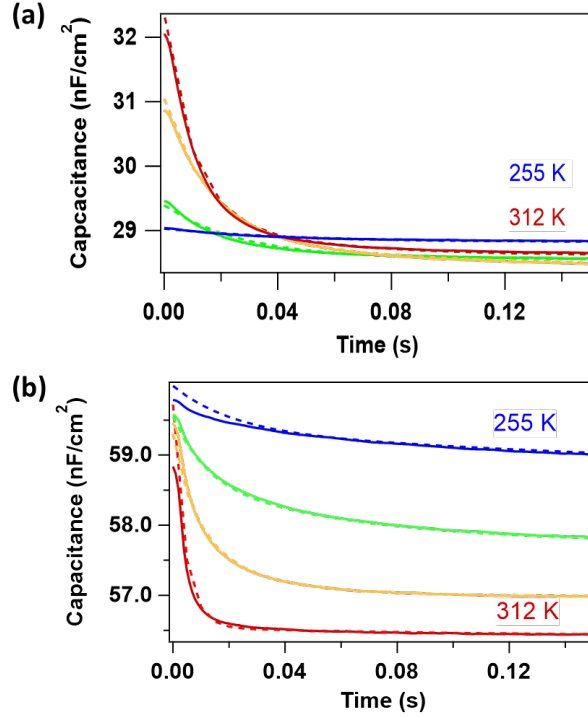
Figure 20: Global fit of the capacitive transients for four different temperatures (red highest to blue lowest) for (a) two exponential fit of a sample with a spin coating time of 5 s and (b) one exponential fit for a sample with a spin coating time of 60 s.

We analyse the three data sets taken at filling voltages of 0.75 V, 1.0 V and 1.1 V for each sample and average over these results to obtain a mean E_a and D. The temperature independent pre-factor D_0 was extracted by the following equation:

$$D_0 = \frac{k_b \, \varepsilon \, \varepsilon_0}{q^2 \, N_A \, c}$$

Where c is the time constant extracted from the fit, while the perovskite permittivity ε and the doping density N_A is extracted from the Mott-Schottky plot, ε_0 is the vacuum permittivity and q is the elementary charge. Now, D_0 can be used to calculate the diffusion coefficient D:

$$D = D_0 \exp\left(\frac{-E_a}{k_b \, T}\right)$$

Where E_a is the activation energy extracted from the fit and for T we used room temperature, 298K. The error for the diffusion coefficient was calculated by the error propagation from c and E_a. Furthermore, the ion concentration N_{ion} can be extracted from the fitted ΔC parameter by the equation:

$$N_{ion} = 2 \, N_A \, \frac{\Delta C}{C(\infty)}$$

Where we use the maximum ΔC value, thus we assume that the maximum reachable ion concentration is related to the maximum difference in capacitance. As an error we use the standard deviation of ΔC over the complete temperature range.

4. Results and discussion

In this chapter we are presenting the results of our study, including grain size, solar cell performance, and ion migration.

4.1. Characterisation of the samples

We synthesis multiple batches of PSC with the method described in section 4.1. Each batch of MAPbBr$_3$ solar cells contains 20 samples, with 4 fully stacked solar cells per spin coating time, and one sample containing only HTL and perovskite, to be able to analyse the perovskite film separately.

4.1.1. Perovskite film characterization

Figure 21 shows the UV-Vis spectrum of two batches, where the optical density is plotted against the wavelength. Both batches show a typical MAPbBr$_3$ UV-Vis spectral shape, including the exciton peak at 520 nm and a rising absorption at smaller wavelength. The rising absorption at 400 nm results from the FTO layer underneath the perovskite thin film.[54] Within one batch the samples with different spin coating times, i.e. different grain sizes, show very similar spectra. Only the film for a spin coating time of 20 s shows a slightly higher absorbance than the others in both batches, which leads to the assumption that this spin coating time might lead to a thicker film formation. When comparing the two batches, B1 and B2, B1 shows in general a higher absorbance than B2, which could indicate a difference in the thickness of the layer of the perovskite films from a difference in precursor concentration.
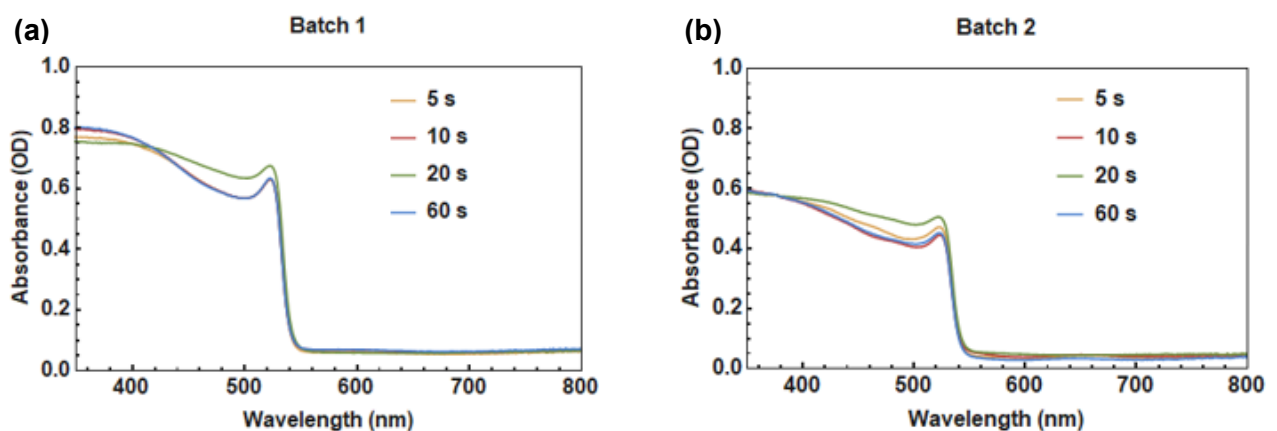

Figure 21: UV-Vis spectrum, absorbance plotted against the wavelength of two different batches (a) batch 1 and (b) batch 2 for all four spin coating times 5 s, 10 s, 20 s, 60 s

To extract the value of the film thickness, which is essential for the subsequent analysis, we take pictures of the cross section of our fully stacked samples in the SEM (see Figure 23). We find that the thickness of the perovskite layer in all our samples is about 300 nm with only minor local variations. We also clearly recognize all different layers in the picture, which confirms that we synthesize uniform films on top of each other.
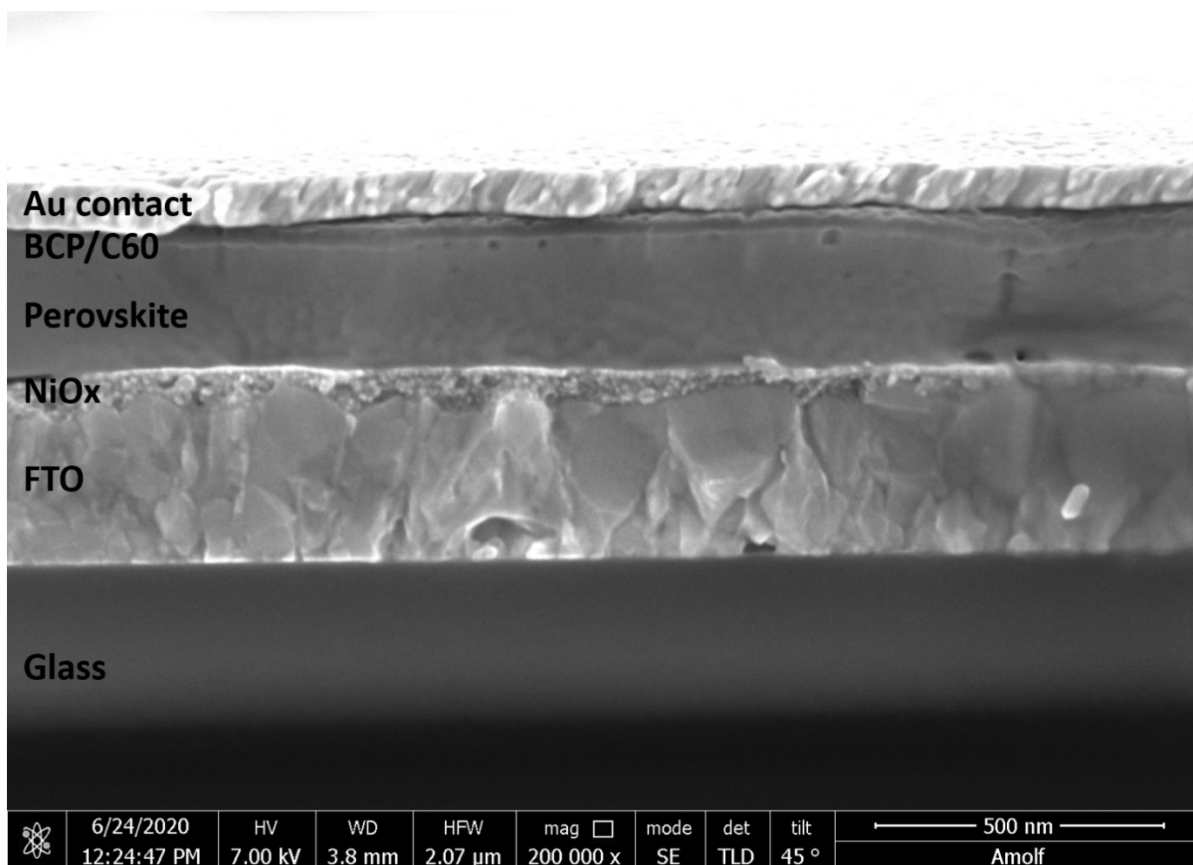
Figure 22: cross section SEM of the fully stacked MAPbBr₃ solar cell sample with a spin coating time of 5 s

To analyse the crystallographic structure and possible impurities of the perovskite film, we record the XRD spectra for each grain size of the two different batches prepared. Figure 23 shows the normalized spectra for comparison. The XRD pattern is consistent with previously obtained patterns in the literature.[55] In both batches, we see the three distinct peaks at an angle of 15, 30 and 46 degree, which are characteristic for $MAPbBr_3$ and correspond to the crystalline cubic (100), (200), (300) planes.[56] Additionally, we see a peak at 38 degrees which we assign to the FTO layer underneath the perovskite thin film.

Figure 23: XRD spectra of two batches for all spin coating times 5 s, 10 s, 20 s, 60 s for (a) batch1 and (b) batch 2

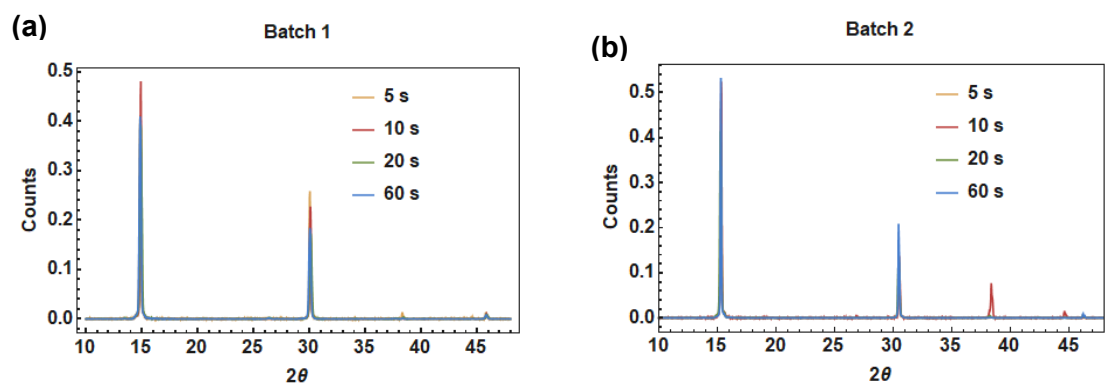### 4.1.2. Grain size distribution

We quantify the grain size after the TID measurement, with optical microscopy images (see figure 24a) analysed with ImageJ. The Figure 24b shows the grain size distribution for the two batches prepared. For both batches the sample with a spin coating time of 5 s has a mean grain size of 13 µm and shows a wide distribution of grain sizes from 5 to 20 µm. The 10 s sample shows a smaller distribution and a main grain size of about 5 µm. The 20 s sample has a main grain size of 2 µm and the 60 s sample has a grain size of 1 µm, both show a very sharp peak, so the distribution is not widely spread. To simplify the discussion, we assign each spin coating time to one (mean) grain size (see Table 3).
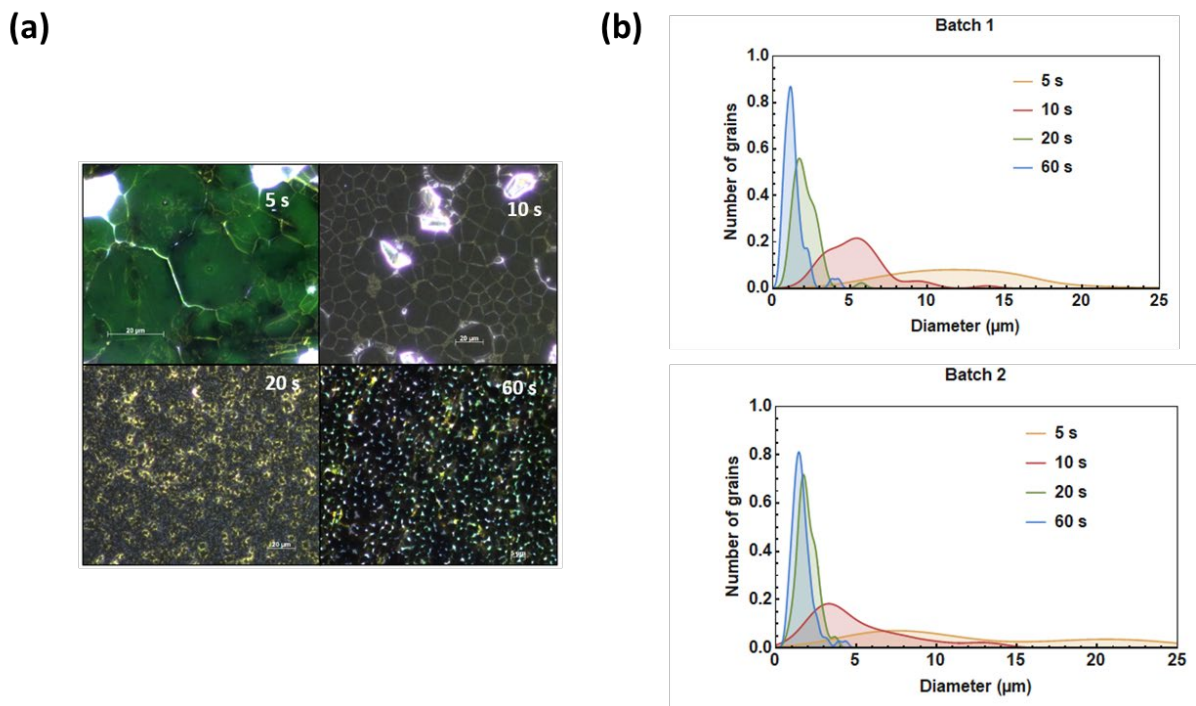

Figure 24: (a) representative optical microscope pictures of the perovskite thin film for all four spin coating times (b) Grain size distribution for all spin coating times of the two batches.

Table 3: assigned grain size to each spin coating time

Spin coating time	5 s	10 s	20 s	60 s
Grain size (µm)	13	5	2	1

4.1.3. Performance of the MAPbBr₃ solar cell

We measured the J-V-curve of our devices, in a solar simulator. Figure 26 shows one example of the measured J-V-curve in the dark (blue curve) and in light (red curve), for the best pixel of the 60 s sample of the first(see Figure 25a) and the second batch (see Figure 25b). Analysing the resistance for the first batch shows that we have a high contribution from the series resistance R_S, which can be seen when looking at the decreased slope between 0.4 V and 0.6 V. For the second batch we assume that the shape of the curve results from a combination of a high R_S and a low R_{SH}, where the R_{SH} leads to an increased slope at the beginning of the curve. The short-circuit current density J_{sc} is higher for the second batch, the open-circuit-voltage V_{oc} is comparable and the fill factor FF is higher in the first batch which results in a higher efficency. In general, for batch 1 we achieve higher efficencies of about 1.9 %, and for batch 2, the highest efficency we reach is 1.6 %. For our simplified design, these are reasonable results, compared to the record efficency of 7.5 % for MAPbBr₃ [57], which includes additional interlayers in between the transporting layers and the perovskite. While the devices have a relativley high series resetance, they still work suffiently well for the TID measurement where this resistent will mainly limit the range of accesible frequencies.
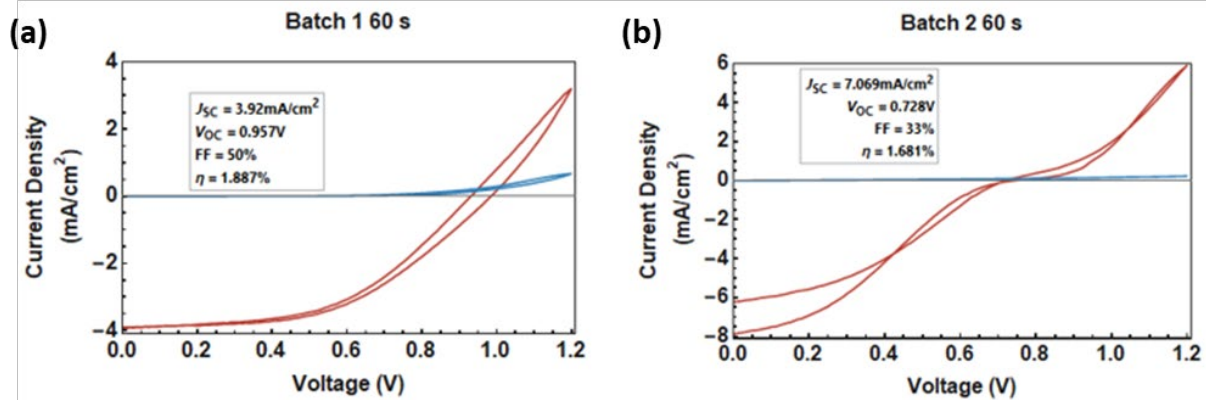
Figure 25: J-V curve measured under a solar simulator (red) and in dark (blue) and characteristic value for the short circuit current J_{SC}, open circuit voltage V_{OC}, fill factor FF and efficiency η for the smallest grain size of two batches with a spin coating time of 60 s

We measure the external quantum efficiency (EQE) to analyse the current generation of the complete device. In our case the first batch shows a sufficiently high EQE of about 45 % (see Figure 26a), which is comparable to previously reported values of about 55%.[58] All grain sizes show a similar EQE except the 10 s sample which has an EQE value of about 30 %. For the second batch, the EQE is lower at about 30 %, also here the 10 s sample shows a lower EQE

39

than the others of about only 10 % (see Figure 27b). Since the photocurrent generation is not important for the TID measurement, this is still a sufficient value.

Figure 26: EQE plotted against the wavelength for two batches for all spin coating times 5 s, 10 s, 20 s, 60 s

4.2. TID measurement and Mott-Schottky analysis

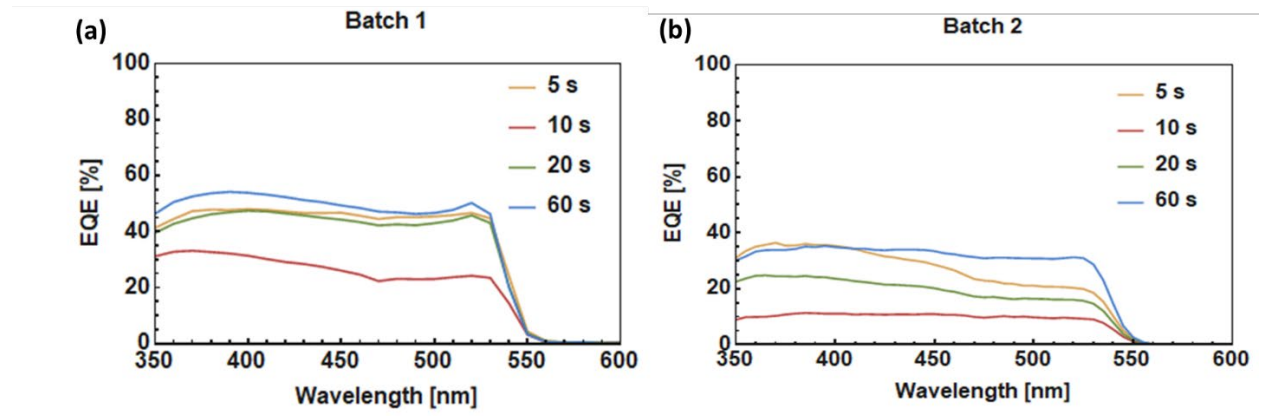To determine the suitable AC-frequency we analyse the TAS data and find three regimes in the impedance curve. For low frequencies ions accumulate at the interfaces which dominates the capacitance.[59] For very high frequencies, the value for the capacitance decreases because of the series resistance of the transport layers. In between these two extremes, there is a plateau of relatively stable capacitance where we can assume the measured capacitance is related to the geometric capacitance of the device, i.e. of the perovskite layer. Therefore, we chose an AC the frequency of 10 kHz (see Figure 27a). We measure the I/V curve(see figure 27b) and C/V curve which we use to make a Mott-Schottky plot (see Figure 27c) to extract several important characteristics of the PSC's such as the build-in voltage V_B, the doping density N_A, and the permittivity ε of the perovskite layer.
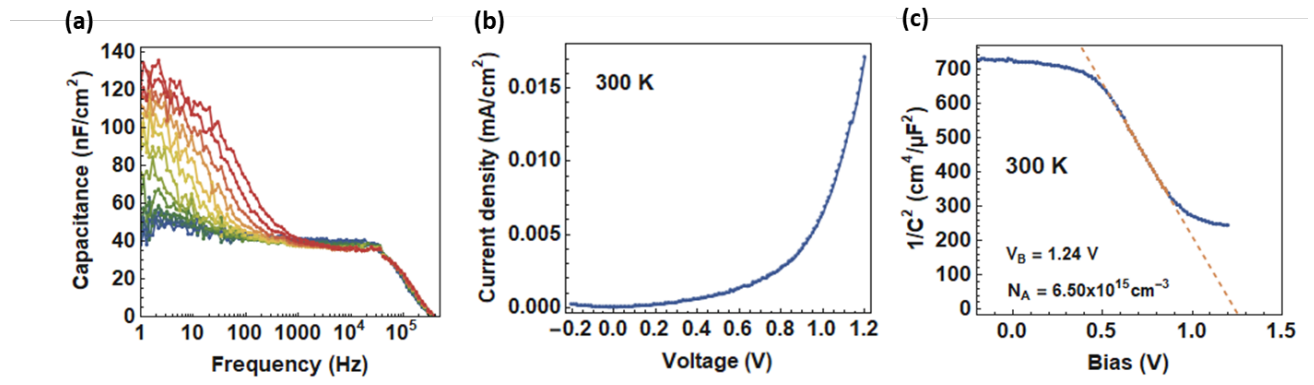

Figure 27: (a) Impedance measurement of a MAPbBr$_3$ solar cell device, from 1 Hz to 500kHz measured from 240 K (blue) to 350 K (red) in steps of 10 K.(b) J/V measurement in reverse mode at 300 K for a spin coating time of 5s and (b) C/V measurement in reverse mode at 300 K for a sample with a spin coating time of 5s, including the calculated values of the built in voltage V_B and doping density N_A

Table 4 shows a summary of the characteristics for all measured samples. The values for the first batch are averaged over two measured samples. The value of the built-in voltage and the permittivity of the perovskite layer is comparable within the first and second batch. The built in voltage is about 1 V, which is in the same range of the built in voltage for MAPbI$_3$ solar cells.[59] The dielectric constant of the perovskite layer in our MAPbBr$_3$ PSC's is in the range of 10 to 20. We note that the permittivity of the perovskite layer is slightly lower than the usually reported value of 20 to 35 in the literature for MAPbI$_3$ PSC's.[59] The calculation of the perovskite permittivity is based on a model considering a parallel plate capacitor. Thus, the value for the permittivity is highly dependent on the thickness of the perovskite layer, which may explain the deviation of our value from other reported values. The doping density is in the range of

10^{15} to 10^{16}, which is lower than the typically assumed doping density of 10^{17} at room temperature.[59] The doping density is highly dependent on the preparation method, thus we use the values extracted from the measured Mott-Schottky plot to calculate the values for the diffusion coefficient and ion concentration of the mobile ions.

Table 4: Table of the values for the built in voltage V_B, doping density N_A and permittivity ε of the perovskite layer for B1 an B2 for all samples with 4 different spin coating times 5s, 10s, 20s, 60s

B 1	V_B (V)	N_A (cm^{-3})	$\varepsilon_{perovskite}$
5s	1.2	$4,3*10^{15}$	12.1
10s	0.9	$5,0 \times 10^{15}$	13.7
20s	1.0	$5,7 \times 10^{15}$	12.3
60s	1.2	$7,7*10^{15}$	14.4

B 2	V_B (V)	N_A (cm^{-3})	$\varepsilon_{perovskite}$
5s	1.0	$1,3*10^{16}$	9.7
10s	0.9	$4,2 \times 10^{15}$	14.9
20s	1.3	$3,4 \times 10^{15}$	18.5
60s	1.2	$4,1*10^{15}$	19.0

The recording of the capacitance transients after the filling pulse always shows a decay for all batches. We assume that we measure p-type perovskites, thus we are measuring an anion migration. The only element in MAPbBr$_3$ which forms anions is bromide, thus we are measuring Br$^-$ migration. When comparing multiple filling voltages, we discover that a minimum voltage is necessary for the ions to move. Figure 28 shows the TID measurement for a representative example from the first batch with a spin coating time of 5 s for a filling pulse voltage of 0.5 V, 0.75 V and 1.0 V. Here we can see that the measurement after applying a 0.5 V pulse shows almost no decay in capacitance while at 0.75 V the decay begins, and at 1.0 V the decay reaches its maximum. This is the case for both batches, accordingly we measure each sample with three filling voltages, 0.75 V, 1.0 V and 1.1 V.
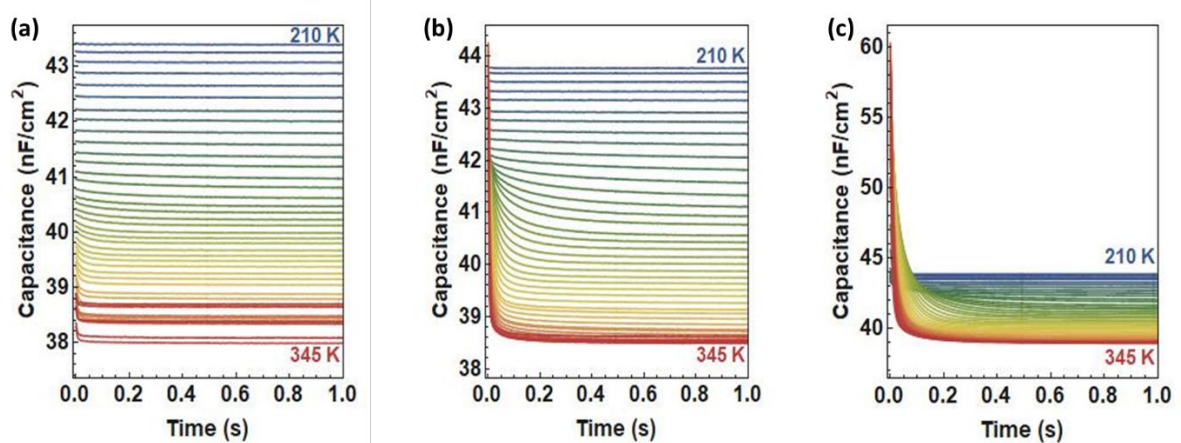

Figure 28: capacitance transients for temperatures ranging from 210 K to 345 K of sample B1 with a spin coating time of 5 s, for (a) 0.75 V, (b) 1.0 V, (c) 1.1 V filling voltage

4.3. Results for the global analysis of the TID data

Figure 29 shows the results for the extracted activation energies (see Figure 29a) and diffusion coefficients (see Figure 29b) of the $MAPbBr_3$ solar cell devices with varying grain size. The values are averaged from two different batches each containing two samples measured at three different filling pulse voltages (0.75 V, 1 V, 1.1 V). For the smaller grain sizes, we fit the transients with one exponential, suggesting a single type of migration process in small-grain cells. For the samples with a grain size of 13 and 5 µm we find two exponentials, representing two different pathways for the Br^- anions to migrate. The values for the activation energy increase with the grain size, from 0.15 eV for the 1 µm grain size cells to 0.28 eV and 0.35 eV for the two pathways of the 13 µm grain size cells. The corresponding diffusion coefficients are overall comparable to each other, ranging from 1 to 2.5 10^{-9} cm^{-2}/s for all grain sizes. We do recognize that for the large grain sizes of 5 and 13 µm, the higher activation energy of the two exponentials we find corresponds to a lower diffusion coefficient and vice versa, suggesting that there are two different migration pathways where one of them is favourable for ions to migrate.
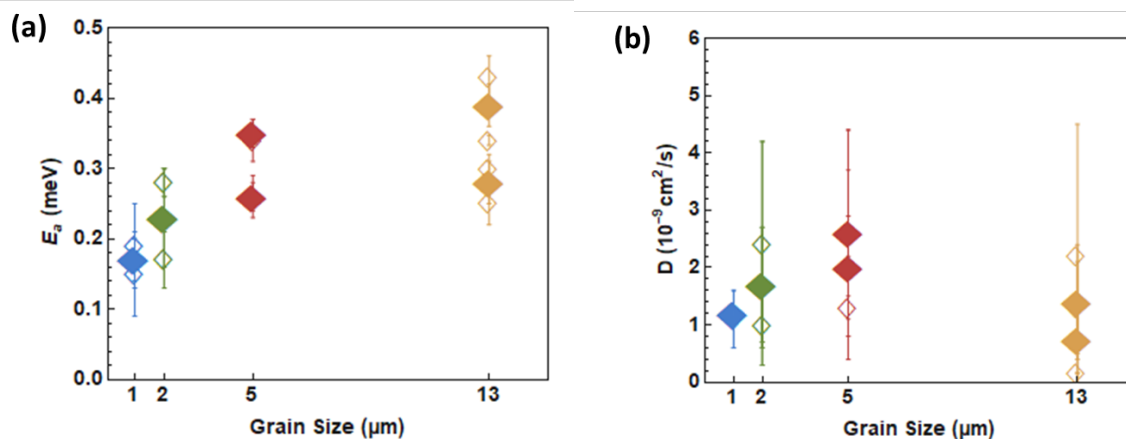
Figure 29: (a) Calculated activation energies E_A and (b) diffusion coefficients D for all grain sizes 1, 2, 5 13 µm where the solid markers represent the average over two batches and the open markers the individual values per batch. For the smaller grain sizes of 1 and 2 um we identify one exponential and for the larger grain sizes of 5 and 13 µm we identified two movements. While the error bars where defined directly by the fit.

To evaluate the ion concentration for the migrating Br^- ions, we plot the fitted values for ΔC against the temperature. Figure 30a shows the fitted ΔC value for a representative sample with large grain size of 13 µm with the two different exponential components identified, and Figure 30b represents the fitted ΔC values for the smallest grain size of 1 µm with the single

exponential component identified. With increasing temperature, the value for ΔC is increasing until a certain point and then decreases again, see for instance the peak at 315 K in Figure 30a. This is because with increasing temperature more ions are moving which leads to an increase in the capacitance difference ΔC. If the temperature gets too high we suggest that there is an additional effect which decreases the amount of ions moving which leads to a decrease of ΔC (see section 4.4 for further discussion). In addition, we calculate the ion concentration of the mobile bromide ions in the perovskite layer. Figure 30c shows the concentration averaged over two batches. The ion concentrations are all in the range of 10^{15} cm^{-3}. Only slightly variations are visible within the different grain sizes.
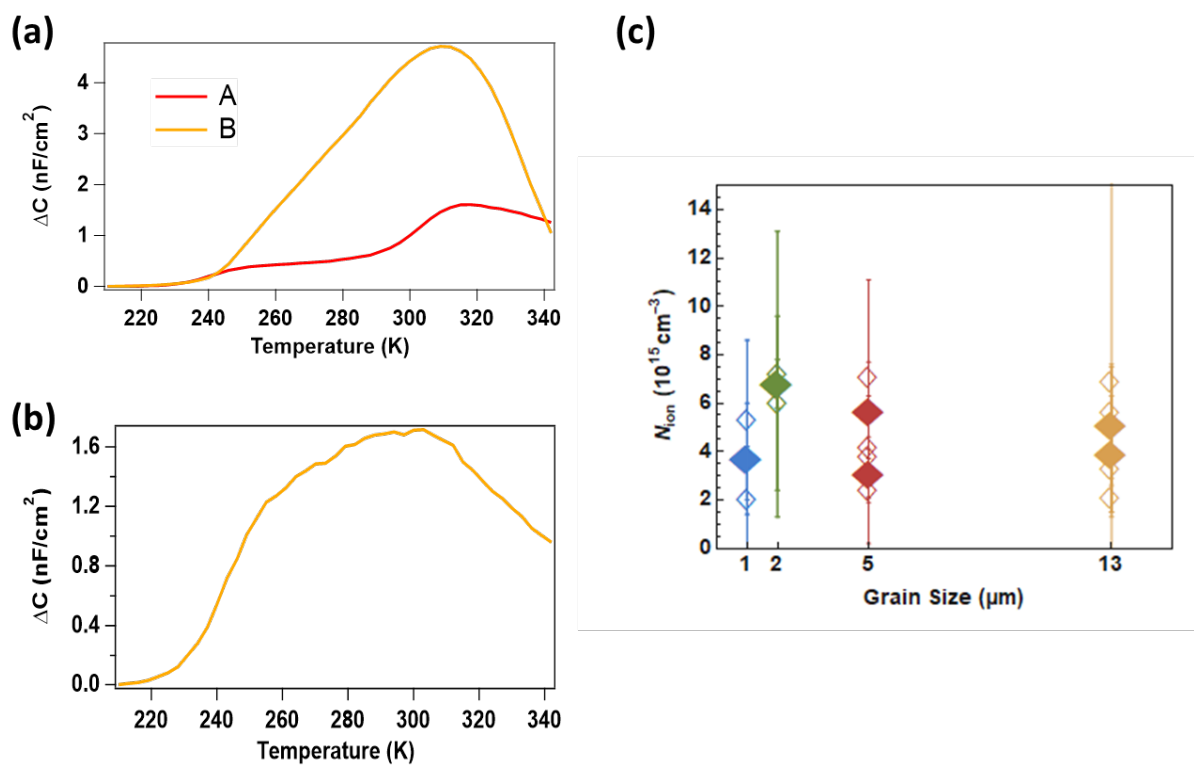
Figure 30: Plot of the fitted ΔC values per temperature for representative samples with (a) 13 um grain size and (b) 1 um grain size and a filling voltage of 0.75V with A and B representing the fitted exponential 1 and 2 for the two larger grain sizes.(c) Ion concentration averaged over two batches for all grain sizes where the solid markers represent the averaged value and the open markers the individual value per batch, while the error bars where calculated from the variance of ΔC over the temperature range.

4.4. Discussion

The overall value of the activation energy agrees with the measured activation energy of vacancy mediated ion migration for Br⁻ in $CsPbBr_3$ from Mizusaki et al.,[60] who measured a value of 0.25 eV. With decreasing grain size, the ratio of grain boundaries to bulk increases, which means that the influence of grain boundaries on ion migration is increased. Thus, the decreasing activation energy for ions to migrate with decreasing grain size supports the previously proposed thesis[5,47,49] that ion migration is enhanced at the grain boundaries. Therefore, we suggest that with a small enough grain size, ions migrate predominantly at the grain boundaries. For the larger grains we found two different exponentials, which should refer to two different ions or two different migration pathways. Since Br⁻ is the only negatively charged ion, the two exponentials must refer to two different pathways of bromide migration. Considering that we see the second ion migration pathway only for samples with a large grain size, we suggest that this pathway could result from ion migration within the grains. This in turn indicates that the other pathway with a lower activation energy refers to migration at the grain boundaries. We suggest that also for small grain sizes, there is ion migration within the grain but less pronounced so that we cannot identify it with our technique. The activation energy for the migration within the grain is higher than for the migration at the grain boundaries, which is in accordance with the results of Shao et al.[49] Additionally the activation energies for the second exponential for the samples with large grain sizes is more comparable to the activation energies for the migration in the samples with small grain sizes of 1 and 2 μm. We suggest therefore that the migrating pathway for the samples with small grain sizes results probably from migration occurring predominantly at the grain boundaries.

The diffusion coefficient of our samples is within a range of 10^{-9} cm², which is the same range as the I⁻ migration in $MAPbI_3$ PSCs measured by Futscher et al.[30] The first exponential, which we assigned to migration at the grain boundaries, shows a higher diffusion coefficient than the second exponential, which we assigned to the migration inside the grain, for large grain sizes of 5 and 13 μm. This strengthens our suggestion that for large grain sizes two pathways of Br⁻ migration are possible, one at the grain boundaries and one inside the grain. The value of the diffusion coefficient stays relatively constant with increasing grain size per ion migration pathway. This means that there must be a compensating term for the increase in activation energy with the grain size. The theoretical formula for the diffusion coefficient, showed in section 3.3.2, shows that there are three possible compensating terms which counteract the increase in the activation energy with increasing grain size, while leaving the diffusion coefficient constant. These terms are, first the increase in ΔS, second an increase in the

attempt-to-escape frequency v_a or third an increase in the jump distance d. We rule out the first possibility because the difference in entropy S would decrease with increasing grainsize. The lower degrees of freedom at grain boundaries leads to a larger entropy difference for an ionic jump, and therefore the entropy difference would decrease when the grains are getting larger not increase. The second possibility is highly unlikely because with less grain boundaries and therefore less open space the distance of an ionic jump is limited to the next defect in the crystal lattice, i.e. it decreases with increasing grain size. The third possibility seems to be likely. The presence of uncoordinated atoms and the open space at the grain boundary suggests weaker bonding between the atoms, which leads to a lower attempt-to-escape frequency at the grain boundaries. This in turn means that the attempt-to-escape frequency would increase with increasing grain size and less grain boundaries. Therefore, we suggest that the attempt-to-escape frequency term compensates for the increase in activation energy for larger grains, so that the diffusion coefficient stays constant at room temperature.

The Br^- concentration is in the range of 10^{15} cm^{-3} for all measured samples. The values for the different grain sizes are relatively constant, which means that the ion concentration stays constant within the range of grain sizes from 1 to 13 µm. We note that the measured ion concentration is within the same range as the measured ion concentration for I^- in $MAPbI_3$ PSC.[30,61,42] However there are also studies which suggest a value three orders of magnitudes higher, for the ion concentration in lead halide PSCs, of about 10^{18} cm^{-3}.[62] These studies assume that the electric field is completely shielded in the perovskite which is not the assumption we make in our study.

According to the temperature dependence of ion migration, the capacitance difference ΔC should increase with temperature until a certain point where it stabilizes. At low temperature, no ions are moving, and where it saturates the maximum possible number of ions are moving. In our data, we see that ΔC is indeed increasing with temperature until a certain point but then decreases again for very high temperatures. This could have several reasons. First, it is possible that the ions are migrating too fast for our set-up to measure them. Secondly, at high temperatures an additional process occurs which influences the concentration of ions which are migrating. We rule out the first hypothesis, because fitting with an additional Instrument Response Function IRF term in the fit function gives no sufficient fit of the transients. The second explanatory statement seems to be more reasonable. We suggest that process could be halide migration into the transport layers as was reported for I^- in $MAPbI_3$. [63,64] This process decreases the concentration of mobile ions inside the perovskite layer for high temperatures.

46

5. Conclusion and outlook

In conclusion, we fabricated $MAPbBr_3$ PSCs with varying grain sizes ranging from 1 to 13 μm. The samples are used to quantify ion migration depending on the grain size, using a capacitance-based technique called transient ion drift TID. The results revealed a negative capacitance difference which means that only Br^- anions are migrating in all samples. Our results showed no evidence for MA^+ migration, in contrast to $MAPbI_3$ solar cells.[30]

For the samples with large grain size, we measure the activation energy for two ion migration pathways, inside the grain and at the grain boundaries. We find only one migration pathway for samples with small grain size, a pathway which we suggest takes place at grain boundaries. One pathway for small grains and two pathways for large grains could help understand the spread of values found in the literature.

The activation energy for the ions to migrate decreases with decreasing grain size, suggesting that the Br^- ion migration is enhanced at the grain boundaries. The diffusion coefficient for the migration pathway at the grain boundaries is larger than for the pathway through the grain, which, strengthens our hypothesis that ion migration is enhanced at grain boundaries. The ion concentration, which is extracted from the capacitance difference, stays rather constant for all grain sizes.

The capacitance difference shows a decreasing feature for high temperatures. Ion migration is a temperature activated process, which is why the ion concentration should increase with temperature until it stabilizes at its maximum, in contrast we see a peak feature. To fully understand the decreasing feature of the ion concentration, the TID should be measured for different interfaces and a larger temperature range.

Ion migration in PSC is one of the main degradation mechanisms. Our results suggest focussing further research on grain boundary passivation and the synthesis of perovskite films with increased grain size, to enhance the stability of lead halide perovskites.

6. References

1. NREL. Best Research-Cell Efficiencies: Rev. 04-06-2020. (2020).

2. Christian Breyer, Dimitri Bogdanov, AShish Gulagi, A. A. On the role of solar photovoltaics in global energy transition scenarios. *Prog. Photovoltaics resarch Appl.* **20**, 1114–1129 (2017).

3. solar-power_en @ ec.europa.eu.

4. Chiang, C. H. & Wu, C. G. Film Grain-Size Related Long-Term Stability of Inverted Perovskite Solar Cells. *ChemSusChem* **9**, 2666–2672 (2016).

5. Nie, W. *et al.* High-efficiency solution-processed perovskite solar cells with millimeter-scale grains. **347**, 522–526 (2015).

6. Futscher, M. H., Gangishetty, M. K., Congreve, D. N. & Ehrler, B. Quantifying mobile ions and electronic defects in perovskite-based devices with temperature-dependent capacitance measurements: Frequency vs time domain. *J. Chem. Phys.* **152**, (2020).

7. Alta, F. & Asu, E. S. NREL Efficiency Chart. *Www.Nrel.Gov* 2020 (2019).

8. Ansari, M. I. H., Qurashi, A. & Nazeeruddin, M. K. Frontiers, opportunities, and challenges in perovskite solar cells: A critical review. *J. Photochem. Photobiol. C Photochem. Rev.* **35**, 1–24 (2018).

9. Chen, Q. *et al.* All-inorganic perovskite nanocrystal scintillators. *Nature* **561**, 88–93 (2018).

10. Van Le, Q., Jang, H. W. & Kim, S. Y. Recent Advances toward High-Efficiency Halide Perovskite Light-Emitting Diodes: Review and Perspective. *Small Methods* **2**, 1700419 (2018).

11. Park, N. G. Perovskite solar cells: An emerging photovoltaic technology. *Mater. Today* **18**, 65–72 (2015).

12. Perera, S. *et al.* Chalcogenide perovskites - an emerging class of ionic semiconductors. *Nano Energy* **22**, 129–135 (2016).

13. Brehm, J. A., Bennett, J. W., Schoenberg, M. R., Grinberg, I. & Rappe, A. M. The structural diversity of AB S 3 compounds with d 0 electronic configuration for the B - cation. *J. Chem. Phys.* **140**, 0–8 (2014).

14. Song, Z., Watthage, S. C., Phillips, A. B. & Heben, M. J. Pathways toward high-

performance perovskite solar cells: review of recent advances in organo-metal halide perovskites for photovoltaic applications. *J. Photonics Energy* **6**, 022001 (2016).

15. De Wolf, S. *et al.* Organometallic halide perovskites: Sharp optical absorption edge and its relation to photovoltaic performance. *J. Phys. Chem. Lett.* **5**, 1035–1039 (2014).

16. Yin, W. J., Shi, T. & Yan, Y. Unique properties of halide perovskites as possible origins of the superior solar cell performance. *Adv. Mater.* **26**, 4653–4658 (2014).

17. Chen, Q. *et al.* Under the spotlight: The organic-inorganic hybrid halide perovskite for optoelectronic applications. *Nano Today* **10**, 355–396 (2015).

18. Geng, W., Zhang, L., Zhang, Y. N., Lau, W. M. & Liu, L. M. First-principles study of lead iodide perovskite tetragonal and orthorhombic phases for photovoltaics. *J. Phys. Chem. C* **118**, 19565–19571 (2014).

19. Gholipour, S. & Saliba, M. *Bandgap tuning and compositional exchange for lead halide perovskite materials*. *Characterization Techniques for Perovskite Solar Cell Materials* (Elsevier Inc., 2020). doi:10.1016/b978-0-12-814727-6.00001-3

20. Wang, R. *et al.* A Review of Perovskites Solar Cell Stability. *Adv. Funct. Mater.* **29**, 1–25 (2019).

21. Urbina, A. The balance between efficiency, stability and environmental impacts in perovskite solar cells: a review. *J. Phys. Energy* **2**, 022001 (2020).

22. Xie, J. *et al.* Improved performance and air stability of planar perovskite solar cells via interfacial engineering using a fullerene amine interlayer. *Nano Energy* **28**, 330–337 (2016).

23. Asghar, M. I., Zhang, J., Wang, H. & Lund, P. D. Device stability of perovskite solar cells – A review. *Renew. Sustain. Energy Rev.* **77**, 131–146 (2017).

24. Eames, C. *et al.* Ionic transport in hybrid lead iodide perovskite solar cells. *Nat. Commun.* **6**, 2–9 (2015).

25. Wei, J. *et al.* Hysteresis analysis based on the ferroelectric effect in hybrid perovskite solar cells. *J. Phys. Chem. Lett.* **5**, 3937–3945 (2014).

26. Bergmann, V. W. *et al.* Real-space observation of unbalanced charge distribution inside a perovskite-sensitized solar cell. *Nat. Commun.* **5**, (2014).

27. Azpiroz, J. M., Mosconi, E., Bisquert, J. & De Angelis, F. Defect migration in methylammonium lead iodide and its role in perovskite solar cell operation. *Energy*

Environ. Sci. **8**, 2118–2127 (2015).

28. Tress, W. Metal Halide Perovskites as Mixed Electronic-Ionic Conductors: Challenges and Opportunities - From Hysteresis to Memristivity. *J. Phys. Chem. Lett.* **8**, 3106–3114 (2017).

29. Nield, V. M., Keen, D. A., Hayes, W. & McGreevy, R. L. Structure and fast-ion conduction in α-AgI. *Solid State Ionics* **66**, 247–258 (1993).

30. Futscher, M. H. *et al.* Quantification of ion migration in CH3NH3PbI3 perovskite solar cells by transient capacitance measurements. *Mater. Horizons* **6**, 1497–1503 (2019).

31. Nandal, V. & Nair, P. R. Predictive Modeling of Ion Migration Induced Degradation in Perovskite Solar Cells. *ACS Nano* **11**, 11505–11512 (2017).

32. Bowring, A. R., Bertoluzzi, L., O'Regan, B. C. & McGehee, M. D. Reverse Bias Behavior of Halide Perovskite Solar Cells. *Adv. Energy Mater.* **8**, 1–7 (2018).

33. Mosconi, E. & De Angelis, F. Mobile Ions in Organohalide Perovskites: Interplay of Electronic Structure and Dynamics. *ACS Energy Lett.* **1**, 182–188 (2016).

34. Li, C. *et al.* Iodine Migration and its Effect on Hysteresis in Perovskite Solar Cells. *Adv. Mater.* **28**, 2446–2454 (2016).

35. Meloni, S. *et al.* Ionic polarization-induced current-voltage hysteresis in CH3NH3PbX3 perovskite solar cells. *Nat. Commun.* **7**, (2016).

36. Haruyama, J., Sodeyama, K., Han, L. & Tateyama, Y. First-principles study of ion diffusion in perovskite solar cell sensitizers. *J. Am. Chem. Soc.* **137**, 10048–10051 (2015).

37. Yuan, Y. *et al.* Photovoltaic Switching Mechanism in Lateral Structure Hybrid Perovskite Solar Cells. *Adv. Energy Mater.* **5**, 1–7 (2015).

38. Pockett, A. *et al.* Microseconds, milliseconds and seconds: Deconvoluting the dynamic behaviour of planar perovskite solar cells. *Phys. Chem. Chem. Phys.* **19**, 5959–5970 (2017).

39. Birkhold, S. T. *et al.* Direct Observation and Quantitative Analysis of Mobile Frenkel Defects in Metal Halide Perovskites Using Scanning Kelvin Probe Microscopy. *J. Phys. Chem. C* **122**, 12633–12639 (2018).

40. Lin, Y. *et al.* Suppressed Ion Migration in Low-Dimensional Perovskites. *ACS Energy Lett.* **2**, 1571–1572 (2017).

50

41. Senocrate, A. *et al.* The Nature of Ion Conduction in Methylammonium Lead Iodide: A Multimethod Approach. *Angew. Chemie - Int. Ed.* **56**, 7755–7759 (2017).

42. Weber, S. A. L. *et al.* How the formation of interfacial charge causes hysteresis in perovskite solar cells. *Energy Environ. Sci.* **11**, 2404–2413 (2018).

43. Frost, J. M., Butler, K. T. & Walsh, A. Molecular ferroelectric contributions to anomalous hysteresis in hybrid perovskite solar cells. *APL Mater.* **2**, (2014).

44. Leijtens, T. *et al.* Carrier trapping and recombination: The role of defect physics in enhancing the open circuit voltage of metal halide perovskite solar cells. *Energy Environ. Sci.* **9**, 3472–3481 (2016).

45. Chen, Q. *et al.* Controllable self-induced passivation of hybrid lead iodide perovskites toward high performance solar cells. *Nano Lett.* **14**, 4158–4163 (2014).

46. Meggiolaro, D., Mosconi, E. & De Angelis, F. Formation of Surface Defects Dominates Ion Migration in Lead-Halide Perovskites. *ACS Energy Lett.* **4**, (2019).

47. Yun, J. S. *et al.* Critical Role of Grain Boundaries for Ion Migration in Formamidinium and Methylammonium Lead Halide Perovskite Solar Cells. *Adv. Energy Mater.* **6**, 1–8 (2016).

48. Yuan, Y. & Huang, J. Ion Migration in Organometal Trihalide Perovskite and Its Impact on Photovoltaic Efficiency and Stability. *Acc. Chem. Res.* **49**, 286–293 (2016).

49. Shao, Y. *et al.* Grain boundary dominated ion migration in polycrystalline organic-inorganic halide perovskite films. *Energy Environ. Sci.* **9**, 1752–1759 (2016).

50. Garcia-Belmonte, G. & Bisquert, J. Distinction between Capacitive and Noncapacitive Hysteretic Currents in Operation and Degradation of Perovskite Solar Cells. *ACS Energy Lett.* **1**, 683–688 (2016).

51. Zhang, Y. *et al.* Charge selective contacts, mobile ions and anomalous hysteresis in organic-inorganic perovskite solar cells. *Mater. Horizons* **2**, 315–322 (2015).

52. Adhyaksa, G. W. P. *et al.* Understanding Detrimental and Beneficial Grain Boundary Effects in Halide Perovskites. *Adv. Mater.* **30**, 1–9 (2018).

53. Lang, D. V. Deep-level transient spectroscopy: A new method to characterize traps in semiconductors. *J. Appl. Phys.* **45**, 3023–3032 (1974).

54. Sheng, R. *et al.* Methylammonium lead bromide perovskite-based solar cells by vapor-assisted deposition. *J. Phys. Chem. C* **119**, 3545–3549 (2015).

55.   Mali, S. S., Shim, C. S. & Hong, C. K. Highly stable and efficient solid-state solar cells based on methylammonium lead bromide (CH3NH3PbBr3) perovskite quantum dots. *NPG Asia Mater.* **7**, e208-9 (2015).

56.   Ji, H. *et al.* Vapor-Assisted Solution Approach for High-Quality Perovskite CH3NH3PbBr3 Thin Films for High-Performance Green Light-Emitting Diode Applications. *ACS Appl. Mater. Interfaces* **9**, 42893–42904 (2017).

57.   Wu, C. G., Chiang, C. H. & Chang, S. H. A perovskite cell with a record-high-Voc of 1.61 v based on solvent annealed CH3NH3PbBr3/ICBA active layer. *Nanoscale* **8**, 4077–4085 (2016).

58.   McFarlane, T. D., De Castro, C. S., Holliman, P. J. & Davies, M. L. Improving the light harvesting and colour range of methyl ammonium lead tri-bromide (MAPbBr3) perovskite solar cells through co-sensitisation with organic dyes. *Chem. Commun.* **55**, 35–38 (2019).

59.   Almora, O., Aranda, C., Mas-Marzá, E. & Garcia-Belmonte, G. On Mott-Schottky analysis interpretation of capacitance measurements in organometal perovskite solar cells. *Appl. Phys. Lett.* **109**, (2016).

60.   Mizusaki, J., Arai, K. & Fueki, K. Ionic conduction of the perovskite-type halides. *Solid State Ionics* **11**, 203–211 (1983).

61.   Birkhold, S. T. *et al.* Interplay of Mobile Ions and Injected Carriers Creates Recombination Centers in Metal Halide Perovskites under Bias. *ACS Energy Lett.* **3**, 1279–1286 (2018).

62.   Bertoluzzi, L. *et al.* In Situ Measurement of Electric-Field Screening in Hysteresis-Free PTAA/FA0.83Cs0.17Pb(I0.83Br0.17)3/C60 Perovskite Solar Cells Gives an Ion Mobility of ~3 × 10-7 cm2/(V s), 2 Orders of Magnitude Faster than Reported for Metal-Oxide-Contacted Perovskite C. *J. Am. Chem. Soc.* **140**, 12775–12784 (2018).

63.   Bi, E. *et al.* Diffusion engineering of ions and charge carriers for stable efficient perovskite solar cells. *Nat. Commun.* **8**, 1–7 (2017).

64.   Yin, X. *et al.* High efficiency inverted planar perovskite solar cells with solution processed NiOx hole contact. *ACS Appl. Mater. Interfaces* **9**, 2439–2448 (2017).